Rajat Srivastava, Matteo Fasano, Shahin Mohammad Nejad,
Hernán Chávez Thielemann, Eliodoro Chiavazzo,
and Pietro Asinari

3 Modeling carbon-based smart materials

3.1 Introduction

Smart materials show changes in their properties in a predictable manner upon application of external stimuli, such as chemical, electrical, thermal, mechanical, magnetic and light ones. Our knowledge about smart materials exists from the era of Roman Empire: there are several evidences that building materials used at that time, mainly mixtures of several compounds including limestone, had self-healing capabilities, since they were able to repair cracks by the simple action of rainwater [1]. Modern smart materials are opening up new opportunities in several fields, for instance, healthcare, defense, waste management and packaging. In fact, these materials are widely used in applications such as sensors, actuators, robots, artificial muscles and drug delivery. Smart materials can be classified based on their responses to the external stimuli, that is, shape memory, piezoelectric, photoresponsive, electroresponsive, magnetoresponsive and thermochromic materials.

Shape memory materials have the unique capability of remembering their original shape after deformation, thereby returning to it upon application of external stimuli such as thermal, mechanical or magnetic variations [2, 3]. These materials have found application in automobiles, aircraft, biomedical devices, robots, civil structures and textiles [3–8]. Shape memory materials can be made out of alloys, ceramics, polymers, hybrid materials or gels. The first shape memory material dates back to 1932, when Arne Ölander first discovered a solid cadmium–gold alloy that, when deformed in a cold state, returned to its original shape upon heating [9]. Nickel–titanium (NiTi) was then a popular shape memory alloy (SMA) discovered by Buehler et al. [10] in 1963, which spread the use of SMA to the first industrial applications. NiTi alloys are preferable in most applications due to their good ductility, corrosion resistance, mechanical stability and biocompatibility [11, 12]. In recent years, carbon-based shape memory polymers attracted attention due to their capability of handling high strain and temperature, their lower density and recovery temperature and their flexibility and recyclability [13–15]. All these superior properties make them interesting shape memory materials, particularly for aerospace and biomedical fields.

Rajat Srivastava, Matteo Fasano, Shahin Mohammad Nejad, Hernán Chávez Thielemann, Eliodoro Chiavazzo, Pietro Asinari, Department of Energy, Politecnico di Torino, Torino, Italy

https://doi.org/10.1515/9783110479133-003

For example, Zhang et al. [16] fabricated multistimuli-responsive shape memory materials based on polymer composites reinforced by graphene nanoplatelets (GNPs), which could be triggered by electrical and infrared stimuli. Figure 3.1 shows the shape memory mechanism actuated by photothermal effect: after a deformation at low temperature (*Shape 2*), the original shape of the GNP-based polymeric material (*Shape 1*) can be recovered upon exposure to infrared radiation [16]. Recently, carbon-based shape memory polymer nanocomposites seem promising candidates for electrical actuators. In fact, polymer nanocomposites filled with carbon nanotubes (CNTs) have shown low electrical resistivity while fast thermal response to applied voltage. These composites can be tailored to specific actuation requests, since a desired shape recovery can be attained by printing CNTs with a specified pattern throughout the polymeric matrix [17].

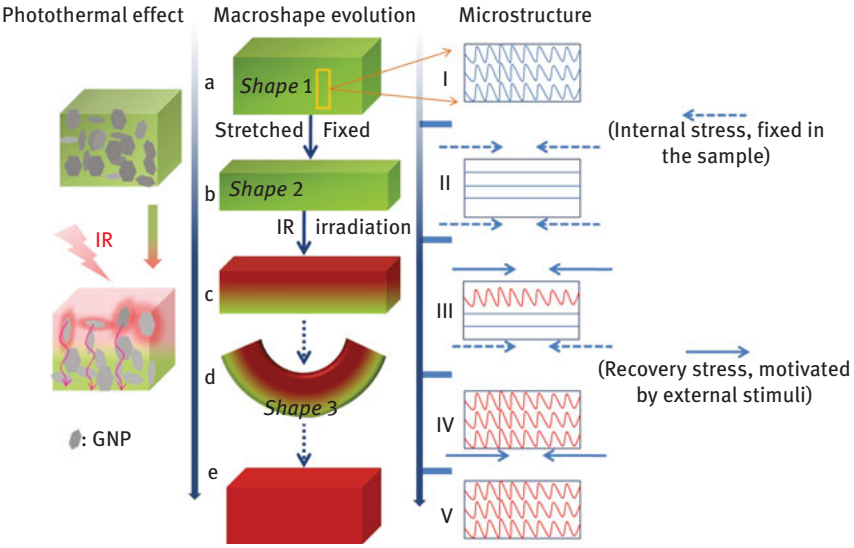

Figure 3.1: Schematic illustration of infrared radiation-actuated shape memory effect of GNP-based polymer blend. Reproduced from Ref. [16] with permission from the Royal Society of Chemistry.

Piezoelectric materials are capable of converting mechanical deformation into electricity, and vice versa [18, 19]. These materials are widely used as sensors, actuators, structural health detectors and energy generators [19–22]. Particularly, there is a growing demand of wearable sensors for monitoring physiological and biomechanical signals in sports and medical applications. However, bulky batteries are currently needed to power these sensors; therefore, smart garments generating their own power by human body motion would be highly beneficial (see Figure 3.2). This requirement can be, for instance, fulfilled by polymeric fiber-based piezoelectric generators, which are flexible and durable as well [23–25].

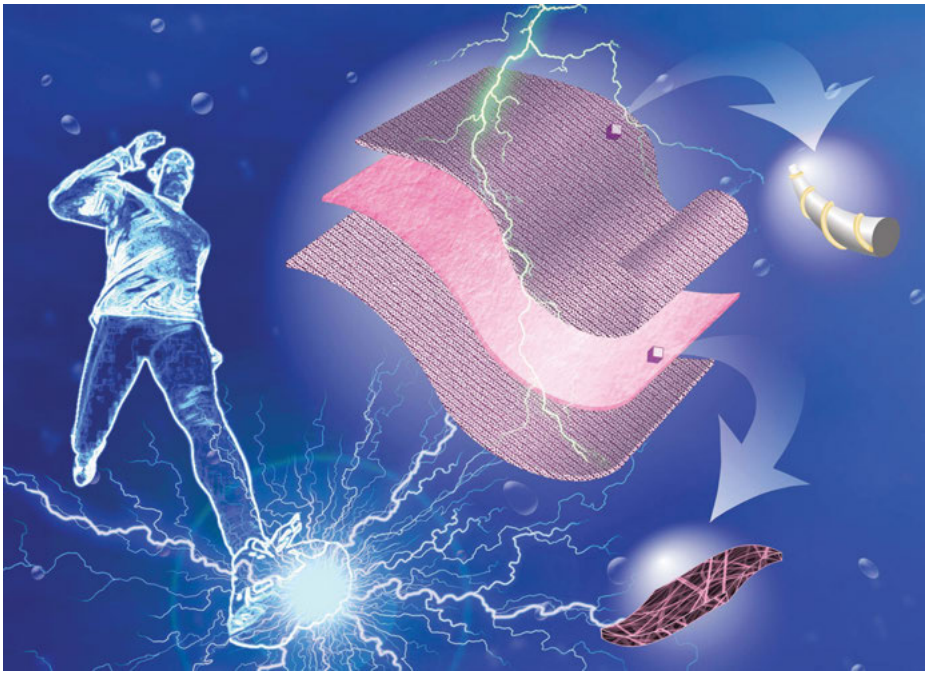

Figure 3.2: Sketch showing power generation from human movement using fiber-based piezoelectric generator. Reproduced from Refs. [23, 26] with permission from the Royal Society of Chemistry.

Zhong et al. [24] fabricated a piezoelectric fiber using cotton threads coated with CNTs and dipped into an aqueous suspension of polytetrafluoroethylene. This carbon-based polymeric piezoelectric fiber utilizes the biomechanical energy from human motion to generate electrical energy, with an average power output of $\sim 0.1\ \mu W/cm^2$, which would be enough to energize wearable sensors or smart shirts (see Figure 3.3).

Photoresponsive materials show changes in their physical and chemical behavior when exposed to light. Usages of these smart materials include anticounterfeiting applications [27], chemical sensors [28], optical switches [29], flexible rewritable optical memories [30] and toys (e.g., doll whose skin get tanned under the sun [31]). The most widely used photoactive agents are azobenzene, spiropyrans, spirooxazines, diarylethenes and fulgides, which are summarily depicted in Figure 3.4.

Recently, Renuka et al. [29] developed an optical switch using multiwalled CNTs (MWCNTs) and azo-based chromophores (Figure 3.5). The electrical conduction of the composite is controlled by azo-based system, which shrinks when exposed to UV irradiation (*cis* isomer), thereby increasing the electrical conduction, because of the reduced tunneling barriers through the MWCNTs. The conduction drops down again when UV irradiation stops, because azo molecules return to their *trans* isomer configuration.

Figure 3.3: Schematic diagram of a smart shirt. Reprinted from Ref. [24] with permission from American Chemical Society.

Lately, *electroactive polymers* (EAPs) are gaining interest because of their unique property to change geometrical/structural properties in response to the application of an electric field. Due to this capability, EAPs can be employed in artificial muscles, sensors, robots, biomedical devices and energy storage systems [33, 34]. *Magnetoresponsive materials*, instead, can be shaped upon the application of a magnetic field. Magnetoresponsive fluids, for instance, can be used to construct dampers with adaptive response and thus enhanced suppression of vibrations. These can be fitted to buildings and bridges to mitigate the detrimental effect of strong winds or earthquakes. Among other applications, magnetoresponsive materials can be used also in nanomedicine [35, 36]. Finally, *thermochromic materials* change color in response to different temperatures. They have been used, for example, in bath plugs that change their color when water is too hot.

Carbon-based polymer nanocomposites seem to be among the most promising candidates for the development of smart materials. However, significant efforts are still needed to design smart materials with specific thermal, mechanical and electrical properties. Since these properties derive by mechanisms coupled from nano- to macroscale, multiphysics simulations could support a more rational research of smart materials with tailored properties. For example, the overall piezoelectric response of carbon-based polymeric smart materials is influenced by several mechanisms, including tunneling of electrons and formation of percolating networks of carbon fillers in the polymer composite [37–39], and should therefore be addressed by linking atomistic to mesoscopic models. In the following sections, the atomistic,

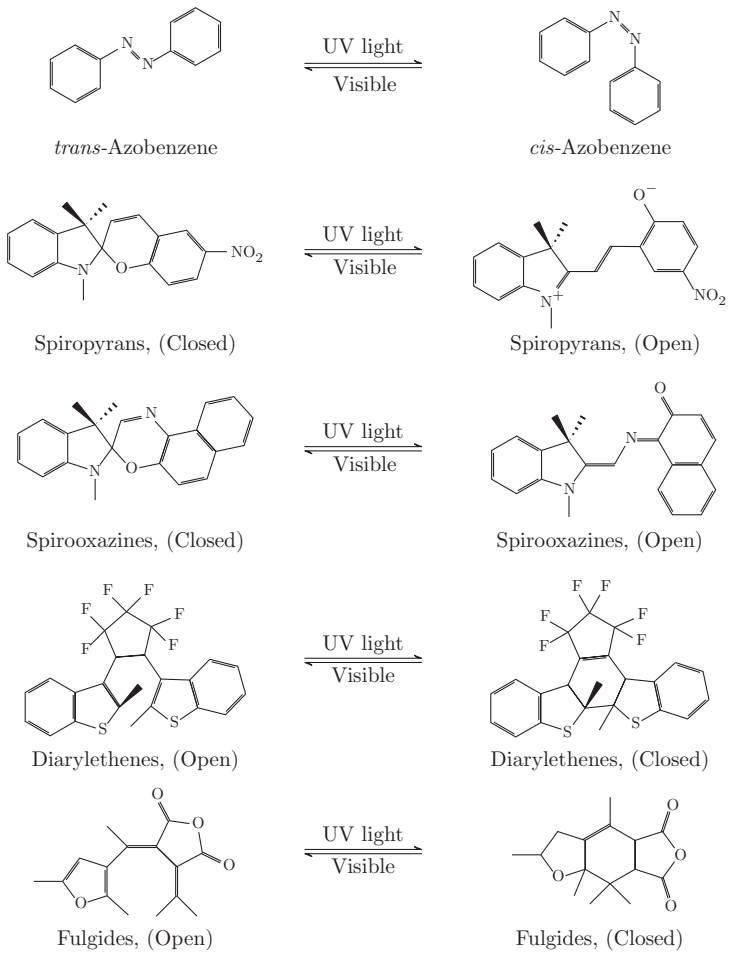

Figure 3.4: Chemical structure of photoresponsive molecules [32].

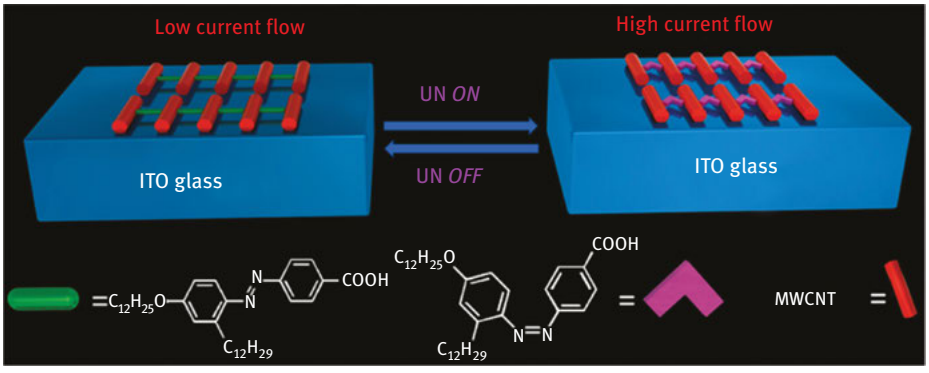

Figure 3.5: Schematic diagram of an optical switch based on MWCNT/azo composite. Reprinted from Ref. [29] with permission from American Chemical Society.

mesoscopic and macroscopic simulation tools that allow to explore the main properties of nanocomposites are extensively presented, and future perspectives of advanced modeling of carbon-based smart materials are discussed.

3.2 Multiphysics modeling

A better understanding of the thermophysical behavior of carbon-based polymer nanocomposites at different length- and timescales could ease the discovery of novel smart materials, and could be facilitated by proper material modeling approaches [40–47]. Advanced modeling approaches to the properties of nanocomposites are based on linking and/or coupling various model types that are applicable at different length- and timescales (see Figure 3.6).

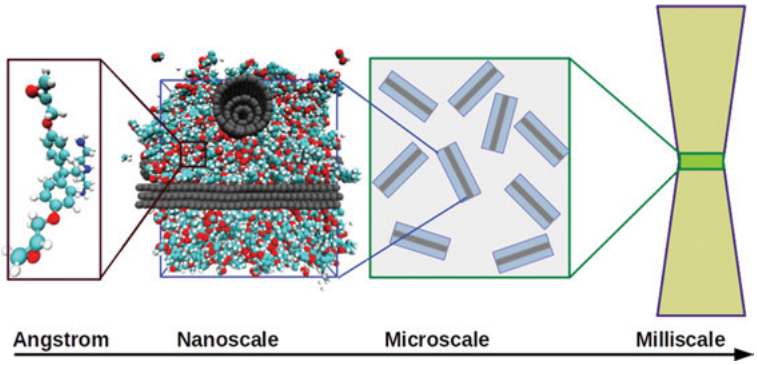

Figure 3.6: Schematic diagram of advanced modeling of polymer nanocomposite across multiple scales.

This situation is ubiquitous in many sectors, where modeling can support the effective development of advanced materials, but the heterogeneity of modeling techniques may prevent to highlight the computational synergies. For this reason, the European Commission published a Review of Materials Modelling (RoMM), now in its sixth edition [48], which provides a classification of materials modeling that enables a coherent description of model types and a standardized documentation of modeling data (called "MODA") of materials. Furthermore, the RoMM contains several examples of MODA documentation applied to a compendium of applications from EU H2020 LEIT NMBP Materials projects. Based on the above review, the European Materials Modelling Council (EMMC, http://www.emmc.info) proposed a CEN Workshop Agreement about "Materials modelling – terminology, classification and metadata" [49], endorsed by more than 15 European organizations with the objective of standardization of terminology, classification and documentation of materials

modeling and simulation. Moreover, the EMMC already proposed a European Materials Modelling Ontology (EMMO) [50]. The EMMO aims at addressing the granularity levels of materials modeling (atomistic, electronic, mesoscopic and continuum), which do not really depend on the scale they are applied to. This is why multiscale modeling is somehow confusing and it would be better to talk about multiphysics modeling.

In particular, at atomistic/molecular level, molecular dynamics (MD) simulations allow understanding the behavior of the constitutive elements of nanocomposites (such as carbon fillers and polymer matrices) and, most importantly, their interaction at the interface [51]. The structural and interfacial characteristics of the constitutive elements of nanocomposites at molecular level are successively employed in coarser modeling descriptions (mesoscopic models). The mesoscopic structure of a smart composite is modeled by a representative volume element (RVE) of the material, and the properties computed at mesoscale can be finally homogenized to evaluate the effective thermophysical properties at macroscopic (continuum) level.

3.2.1 Atomistic models

Thermophysical properties of carbon-based nanocomposite materials are mainly governed by the interaction between nanofillers and surrounding matrix at molecular level. MD simulations are typically the most adequate tool to study such atomistic phenomena. In this section, the process of building the molecular geometry of nanocomposite is first discussed; then, the MD protocols for assessing thermal, mechanical and electrical properties are described, and main results from the literature are presented.

Building the atomistic setup

While the atomistic structure of carbon nanofillers (e.g., nanotubes, nanoplatelets and nanoribbons) can be conveniently generated by tools available in the literature [52–54], one of the major challenges in simulating polymer-based nanocomposites at the molecular level is to accurately describe the structure of polymeric matrix. Curing is a chemical reaction that happens between the components of thermosetting plastics (e.g., epoxy resins), namely the resin and hardener, which result in a final crosslinked (cured) structure. MD methods possess an inherent advantage over continuum approaches, since they are able to accurately simulate the mechanisms underlying curing reaction. Schulz and Frisch [55] first attempted to model curing procedure at the molecular level. They employed a lattice Monte Carlo simulation method to understand the reaction kinetics of curing process in terms of degree of polymerization and molecular weight distribution. Later works also included topological information

of polymer networks in the description of curing process, therefore allowing the simulation of thermomechanical properties of epoxy resins by MD simulations [56–64].

Protocols for simulating the curing process and creating the atomistic setup of epoxy resins can be classified into two groups: (1) single-step methods, where all the potential chemical bonds between reactive sites within a specified cut-off distance are formed at once; (2) multistep approaches, where reactive pairs within a spatial distance are cross-linked together and the resulting structure relaxed by MD, iteratively, until the desired curing degree is met. Generally, single-step approaches lead to large artificial strains in the cured structure; whereas, multistep methods – even though they are more computationally expensive – provide structures closer to real curing reactions, since they operate through intermediate MD relaxations.

Jang et al. [64] compared the performance of these two approaches on a system consisting of bisphenol A diglycidyl ether (DGEBA) epoxy and poly(oxypropylene) diamine (POP) curing agent. In the single-step method, a Monte Carlo algorithm was adopted to allocate cross-linking bonds. For the multistep algorithm, an initial cut-off radius of 10 Å was assigned, and covalent bonds between all pairs of potentially reactive atoms within the cut-off radius generated. After that, the partially cured system was relaxed in the NPT and NVE ensembles, respectively. In addition, the partial charges of atoms were adjusted to neutralize the net charge in the system. Finally, in the case that no reactive pairs remained within the current cut-off radius, the reaction cut-off radius was increased iteratively. The thermal (thermal expansion, heat capacity and glass transition temperature), structural (dihedral angle distributions, radial distribution functions, minimum inter-nitrogen contour length distributions and fragment molecular weight distribution) and mechanical (Young's modulus) properties of the systems cured by either single- or multistep approach were then compared. Results showed that the fragment molecular weight distribution was different in the two cases, since fewer and larger fragments were obtained with the single-step approach; nevertheless, the other properties had no significant dependency on the choice of cross-linking method.

Thermal properties

Thermal conductivity

The thermal conductivity (λ) of nanostructured materials can be estimated by either equilibrium MD (EMD) or nonequilibrium MD (NEMD) simulations. It is noteworthy to mention that EMD simulations are best to study homogeneous systems, whereas NEMD techniques are more suitable for heterogeneous systems [65]. Green-Kubo formulation underlies EMD simulations, since it relates λ with the fluctuations of thermal current via the fluctuation-dissipation theorem [66, 67]:

$$\lambda = \frac{1}{Vk_B T^2} \int_0^\infty \langle \mathbf{J}(t)\mathbf{J}(0)\rangle dt, \tag{3.1}$$

where k_B is the Boltzmann constant, T and V are the temperature and volume of the system, respectively. In addition, $\mathbf{J}(t)$ is the heat current vector at time t and $\langle \mathbf{J}(t)\mathbf{J}(0)\rangle$ is the heat current autocorrelation function. In terms of MD entities, the heat current vector is commonly defined as

$$\mathbf{J}(t) = \frac{d}{dt} \sum_{i=1}^{N} E_i \mathbf{r}_i, \tag{3.2}$$

being $\mathbf{r}_i$ and E_i the position and total energy of atom i, respectively. E_i can be computed by summing up kinetic and potential energies of the atom, namely

$$E_i = \frac{1}{2} m_i |\mathrm{v}_i|^2 + \frac{1}{2} \sum_{j \neq i}^{N} U_p(r_{ij}), \tag{3.3}$$

where m_i and $\mathbf{v}_i$ indicate mass and velocity of atom i, respectively. $U_p(r_{ij})$ is the total potential energy of atom i, which depends on the type of bonded and non-bonded interaction potentials used in the simulations and r_{ij} is the distance between atoms i and j.

For example, Kumar et al. [68] used EMD to study the correlation between λ of cross-linked epoxies (DGEBA resin, 4,4′-diaminodiphenyl sulfone - DDS hardener) and temperature. Results demonstrate that the inclusion of long-range Coulomb interaction corrections leads to a better agreement between modeling and experimental results. Sirk et al. [69], instead, employed MD simulations to study the effect of epoxy composition on its thermal, structural and volumetric properties. Different cross-linked networks including DGEBA resin and various mixtures of flexible (POP) and stiff (MCA, 4,4′-Methylenebis(cyclohexylamine)) curing agents were built. They found out that the flexibility of cross-linker has considerable impact on the thermal and volumetric characteristics of the cross-linked network, especially at temperatures close to glass transition. Fasanella and Sundararaghavan [70] adopted the EMD approach to study the effect of temperature and functionalization on λ of DGEBA + DDS epoxy, possibly reinforced by single-walled CNTs (SWCNTs). In particular, the thermal conductivity was computed both perpendicularly and along the main axis of the nanotube. Results showed that, for what concerns the direction perpendicular to the CNT axis, the λ of pristine SWCNT/epoxy nanocomposites is lower than the neat epoxy one, whereas an improved thermal performance is shown for functionalized SWCNT/epoxy nanocomposites (see Figure 3.7). In addition, a significant enhancement in the λ along nanotube axis has been observed in the case of pristine SWCNT/epoxy in comparison to both neat epoxy and functionalized SWCNT/epoxy nanocomposite (see the inset in Figure 3.7).

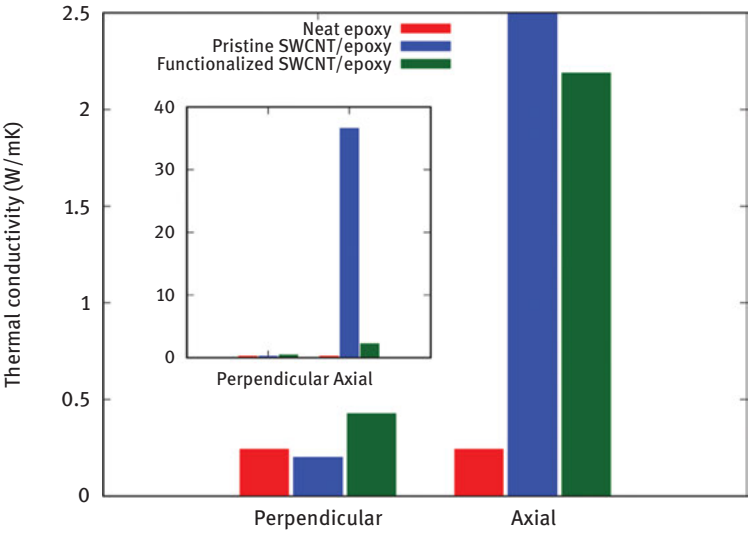

Figure 3.7: Average thermal conductivity in the temperature range of 220–420 K in the perpendicular and axial directions with respect to the nanotube axis for different simulated nanocomposites. Adapted with permission from Springer Nature [70].

NEMD methods for computing thermal conductivity of nanostructured materials are based on Fourier's law. For example, the thermal conductivity of an isotropic system with temperature gradient along z direction can be found as [71]

$$\lambda_z = -\frac{q_z}{dT/dz}, \tag{3.4}$$

where $q_z = Q_z/A$ is the specific heat flux, namely, the heat flux Q_z transferred through the surface A along the direction z. In addition, dT/dz is the steady-state temperature gradient along z-axis. The temperature profile throughout the simulation domain can be computed after dividing the box into N slabs (depending on the system size) along the desired direction. Equation (3.4) can be exploited in nonequilibrium simulations to compute λ according to two possible approaches.

The first approach is typically called NEMD (see an example in Figure 3.8), where a temperature gradient is imposed across the extremities of computational system. This is achieved by a proper design of regions with either high (red atoms in Figure 3.8) or low (blue atoms in Figure 3.8) controlled temperature. To sustain the temperature gradient during the simulation, energy is constantly supplied and extracted from the high- and the low-temperature regions by thermostats, respectively. Such addition or extraction of energy in the hot or cold regions is generally carried out by modifying the kinetic energy of atoms through a velocity rescaling procedure. The instantaneous local kinetic temperature (T_i) in each slab can be computed as

$$T_i = \frac{1}{3N_i k_B} \sum_{k=1}^{N_i} m_k |\mathbf{v}_k|^2, \tag{3.5}$$

where N_i is the number of atoms in the ith slab and m_k the mass of the kth atom. The energy exchange between hot and cold regions at steady state causes a specific thermal flux (q_z) through the system, which can be calculated as

$$q_z = \frac{Q_z}{2A} = \frac{1}{2A\Delta t} \left\langle \frac{1}{2} \sum_{k=1}^{N_B} m_k (|\mathbf{v}'_k|^2 - |\mathbf{v}_k|^2) \right\rangle, \tag{3.6}$$

where N_B is the number of atoms in the thermostated region. Besides, $\mathbf{v}_k$ and $\mathbf{v}'_k$ represent the atomic velocities in the thermosetted regions (hot or cold regions) before and after rescaling, respectively. Note that, in the considered geometry (Figure 3.8), the heat flux in eq. (3.6) is divided by 2 due to the symmetrical simulation box.

The second approach is named as reverse NEMD (RNEMD), and it was originally conceived by Müller-Plathe [72]. The main difference between RNEMD and NEMD methods is that the former generates nonequilibrium conditions through the computational domain by fixing heat flux (which gives rise to temperature gradient), while the latter by fixing the temperature gradient (which gives rise to heat flux). In case of RNEMD, the heat flux is induced by interchanging the atomic velocities between hot and cold regions. In the hot region, the coldest atom is selected and its velocity (v_{cold}, red region in Figure 3.8) is exchanged with the velocity of hottest

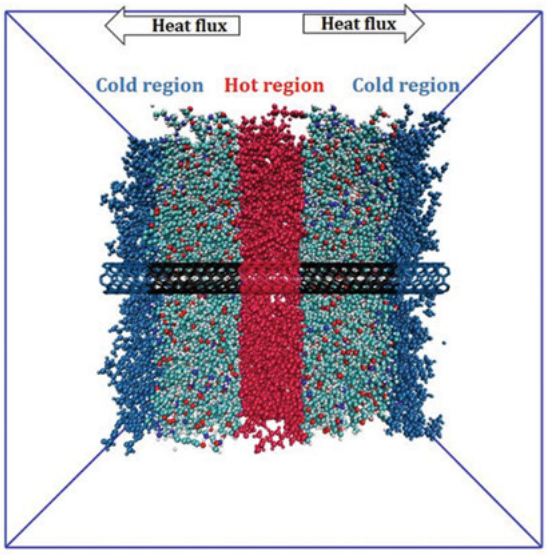

Figure 3.8: Specification of hot and cold baths for computing the thermal conductivity of a carbon-based nanocomposite by NEMD simulations.

atom in the cold region (v_{hot}, blue regions in Figure 3.8). This process eventually leads to an artificial specific heat flux (q_z) flowing from cold to hot regions. All velocity interchange procedure (i.e., *transfers*) follows the total energy conservation law; therefore, at steady state, equal amount of energy per area and time is induced from hot to cold regions via heat conduction, namely

$$q_z = \frac{1}{2A\Delta t} \sum_{transfers} \frac{m}{2} \left(|\mathrm{v}_{hot}|^2 - |\mathrm{v}_{cold}|^2 \right). \tag{3.7}$$

The most significant advantage of RNEMD over classical NEMD is the fact that heat flux, which is a slowly converging quantity with respect to temperature, is fixed from the beginning of simulation. Therefore, in general, RNEMD approaches provide faster convergence of λ computation with respect to classical NEMD ones.

Interestingly, Varshney et al. [73] evaluated the thermal conductivity of a cross-linked network of EPON-862 and curing agent W (diethyltoluenediamine, DETDA) using both EMD and NEMD approaches. In the case of EMD, a cubic simulation box ($53.6 \times 53.6 \times 53.6$ Å^3) was employed; in the case of NEMD, a thin slab with large aspect ratio along the heat flow direction ($21.4 \times 21.4 \times 373.3$ Å^3) was considered instead. The results obtained by both methods were in good agreement with experiments, even though EMD led to a slight overestimation of λ. Mortazavi et al. [74] employed NEMD to estimate the thermal conduction in graphene-reinforced nanocomposites. In their study, epoxy consisted of DGEBA resin and DETA (diethylenetriamine) or DDS curing agents. They found that the thermal conductivity of a single-layer graphene immersed in the epoxy matrix at atmospheric pressure and room temperature decreases by around 30% with respect to the value of pristine graphene, while the type of hardener has no considerable effect. Furthermore, they also investigated the impact of pressure and epoxy-graphene covalent bonds on λ of graphene: no significant change in the λ of graphene was observed by increasing the pressure up to 14 GPa, while the formation of 5% covalent bonds led to 65% reduction in the thermal conductivity of graphene. Clearly, such methodologies can be successfully adopted in a large variety of polymeric matrices: for example, Alaghemandi et al. [75] used RNEMD to investigate the λ of SWCNT–polyamide (PA) nanocomposites along both parallel and perpendicular directions with respect to the nanotube axis, finding a good agreement with experiments [76, 77].

Thermal boundary resistance

The thermal boundary resistance, also known as Kapitza resistance or interfacial thermal resistance (R_k) [78], at filler–filler and filler–matrix interfaces is one of the most significant bottlenecks in the overall thermal conduction through polymer nanocomposites [79, 80]. This thermal resistance arises mainly from the weak van der Waals interactions between adjacent fillers, and between fillers and the surrounding matrix.

Such weak interactions considerably hinder the specific heat flux (q) across the interface due to phonon scattering, which in turn results in a localized interfacial temperature jump (ΔT). The inverse of thermal boundary resistance, also known as thermal boundary conductance, $G_k = 1/R_k$, is defined as

$$G_k = \frac{q}{\Delta T}. \tag{3.8}$$

MD simulations are typically used to investigate thermal boundary resistance, since it arises from atomistic details of interfaces. Generally, two NEMD approaches have been used in the literature to study interfacial thermal properties of nanocomposites [81].

In the first approach, the simulated system is divided into multiple slabs according to the geometrical characteristics of the box. On the one side, a constant heat flux is added to the atoms of nanofiller (heat source); on the other side, a constant heat flux is removed from the outermost region of the computational domain occupied by the matrix (heat sink). This thermal power could be extracted or introduced by means of a velocity rescaling procedure, which must conserve the total linear momentum of the system. As an example, this method was adopted to compute the thermal boundary resistance between the CNT and octane liquid depicted in Figure 3.9. In those simulations [81], the continuous addition (CNT) and extraction (outermost region occupied by octane) of a constant heat flux leads to a steady-state temperature profile throughout the system, where the average temperature in each

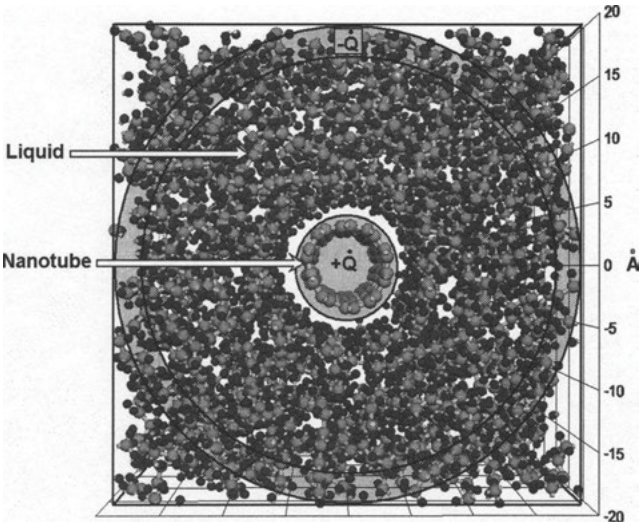

Figure 3.9: Schematic of division of carbon nanotube/octane system into concentric cylindrical slabs to investigate thermal interfacial effects. Reprinted from Ref. [81] with the permission of AIP Publishing.

slab can be computed by eq. (3.5). An example of temperature profile measured in this system is shown in Figure 3.10: the average temperature of the CNT is around 575 K, while the liquid temperature ranges from 320 K (close to the CNT surface) down to 300 K (heat sink). The significant temperature drop at the nanotube–octane interface proves the existence of Kapitza resistance, which is then computed by eq. (3.8) since both q and ΔT can be extracted from simulations.

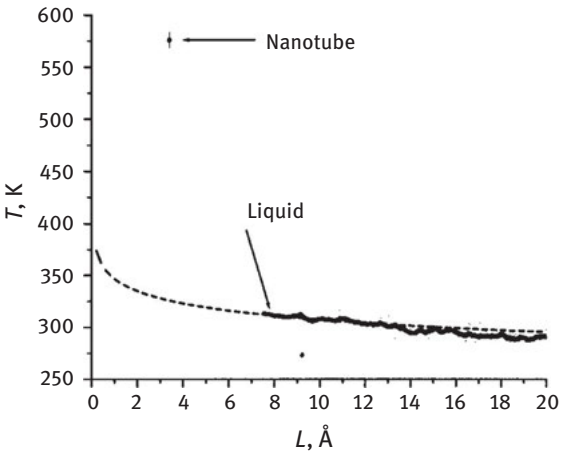

Figure 3.10: Relation between the temperature gradient and distance from the center of CNT at constant heat flow (see configuration in Figure 3.9). Reprinted from Ref. [81] with the permission of AIP Publishing.

In the second approach, the whole system is first equilibrated at the initial temperature $T(0)$; after that, the filler is heated up to a predetermined temperature $T_f(0) = T(0) + \Delta T(0)$, while the matrix temperature is kept constant at the $T_m(t) = T(0)$ value. Such a temperature gradient can be determined by a proper distribution of thermostats in the computational domain. The system is then allowed to relax without any heat source or sink. As depicted in Figure 3.11, the temperature difference between the filler and the surrounding matrix $(\Delta T(t) = T_f(t) - T_m(t))$ tends to decay exponentially with time according to the Newton's law of cooling, namely

$$\Delta T(t) = \Delta T(0) \exp\left(-\frac{t}{\tau}\right). \tag{3.9}$$

If the conduction resistance of the filler is considerably lower than the matrix one (which is typically the case of carbon nanofillers), the characteristic decay time (τ) can be related to the area of filler–matrix interface (A_{int}), the filler heat capacity (c) and the (R_k) at filler–matrix interface as [82]

$$R_k = \frac{A_{int}\tau}{c}. \tag{3.10}$$

Due to the paramount importance of heat transfer across nanoscale interfaces on the effective thermal properties of nanocomposites, several researches have used MD simulations to achieve a mechanistic understanding of the parameters that could affect thermal boundary resistance, such as curing degree of polymeric matrix, surface functionalization of fillers and presence of covalent or noncovalent bonds between fillers and the surrounding matrix [83–100].

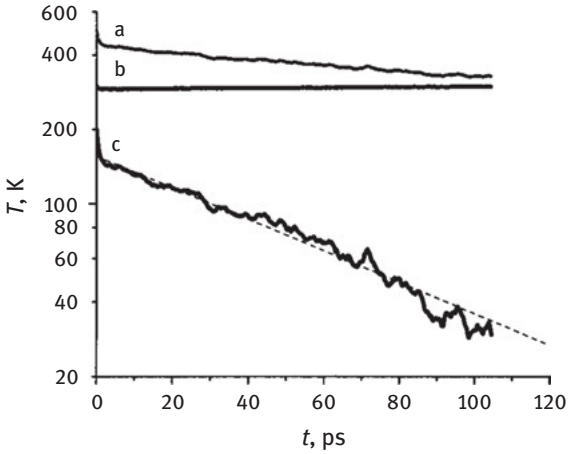

Figure 3.11: Instantaneously heated nanotube at a desired temperature is allowed to relax without heat source or sink, then (a) the temperature of the CNT, (b) liquid temperature and (c) difference between the temperature of CNT and liquid as a function of time are shown (see configuration in Figure 3.9). Reprinted from Ref. [81] with the permission of AIP Publishing.

As an example, Varshney et al. [83] analyzed by MD simulations a nanocomposite made of epoxy polymer (EPON-862/DETDA) reinforced with SWCNTs. They reported a 20% enhancement in the G_k at filler–matrix interface by increasing the curing degree of epoxy. Such behavior was explained by the increased structural rigidity and nonbonded interactions of the cured epoxies, since the curing process generates a denser matrix structure. Huang et al. [94], instead, investigated the impact of covalent bonds (cross-links) between SWCNT and PEK (poly ether ketone) on the thermal boundary conductance at their interface. Considering a simulation domain similar to the one in Figure 3.9, the number of cross-links between SWCNT and PEK was changed in the range 0–80 (0% – 6.25% functionalization degree), and the G_k was then computed in each case. Results in Figure 3.12 show that the temperature jump at CNT–PEK interface decreases with the number of cross-links; thus, G_k increases from 23.58 (no cross-links) to 236.44 MW/m^2 K (80 cross-links). Finally, Wang et al. [89] employed RNEMD to determine how different surface functionalizations of graphene could affect the

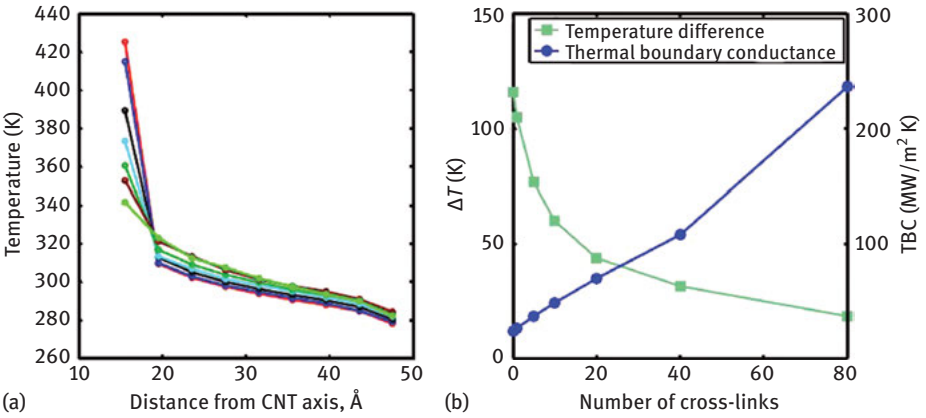

Figure 3.12: (a) Radial temperature distribution in the system under steady-state condition for seven simulated cases: no cross-links (red, 0%), 1 cross-link (blue, 0.08%), 5 cross-links (black, 0.39%), 10 cross-links (cyan, 0.78%), 20 cross-links (dark green, 1.56%), 40 cross-links (brown, 3.12%) and 80 cross-links (green, 6.25%). (b) Temperature difference and thermal boundary conductance at the CNT–PEK interface for different studied cases. Reprinted from Ref. [94] with the permission of AIP Publishing.

interfacial thermal resistance at graphene–polymer interface. To this aim, various types of covalent (butyl, carboxyl and hydroxyl) and noncovalent (1-pyrenebutyl, 1-pyrenebutyric acid and 1-pyrenebutylamine) functional groups were considered at different coverages, namely, the ratio between the number of functional groups to the total number of carbon atoms in the graphene sheet. Furthermore, the effect of isotope doping and acetylenic linkage in graphene was also assessed. Simulation results for covalent and noncovalent functionalizations are reported in Figures 3.13 and 3.14, respectively. It is noteworthy to mention that the thermal boundary resistance values in these figures are normalized using the value of R_k in the case of no functionalization on graphene, that is, $R_{k0} = (0.713 \pm 0.036) \times 10^{-8}$ m^2 K/W. While both increasing covalent and noncovalent functionalizations led to R_k decrease, no significant effects were instead observed with isotope doping or acetylenic linkages in the graphene filler [89].

Mechanical properties

MD simulations are also useful to compute mechanical properties of composite materials, such as the elastic moduli and the whole stress–strain response of a nanometric specimen [101, 102]. Discrepancies between MD and experimental results may be due to the faster strain rate simulated, the effect of dislocations at higher scales, the local high variability of temperature and the possible unwanted residual stresses from cross-link process [103].

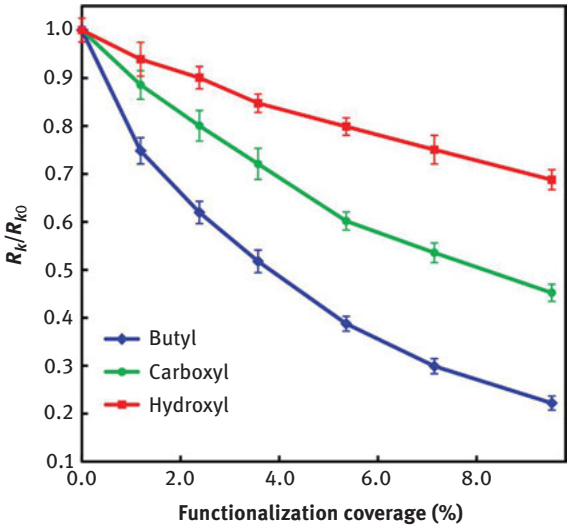

Figure 3.13: Dependence of the relative thermal boundary resistance on coverage percentage of different covalent functional molecules. Reprinted from Ref. [89] with the permission of American Chemical Society.

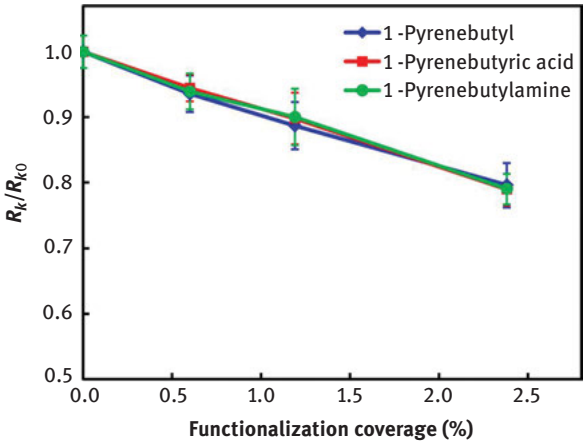

Figure 3.14: Dependence of the relative thermal boundary resistance on coverage percentage of different noncovalent functional molecules. Reprinted from Ref. [89] with the permission of American Chemical Society.

In general, the elastic properties of a material along one specific direction can be quantified by the Young's modulus (E_m) as

$$\sigma = E_m \varepsilon, \tag{3.11}$$

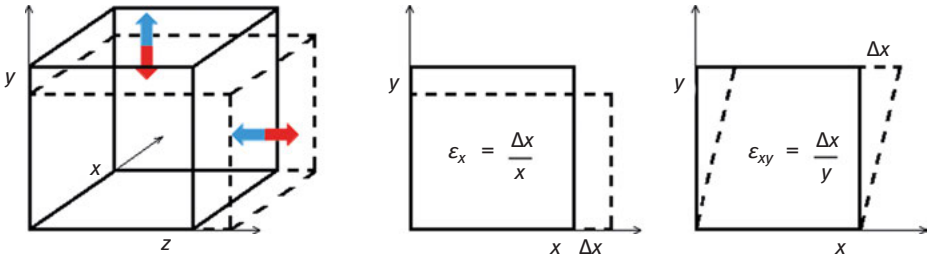

Figure 3.15: Longitudinal and shear deformation of a simple volume of material.

where the stress (σ) is a measure of the average force applied over an equivalent area (F/A), and the strain (ε) is the ratio of deformation with respect to the initial length (see Figure 3.15). Such relation can be generalized to three-dimensional space to relate all the components of the stress and strain tensors (generalized Hooke's law):

$$\sigma_{ij} = C'_{ijkl}\,\varepsilon_{kl}, \tag{3.12}$$

where C'_{ijkl} are the components of the fourth-order stiffness tensor of the considered material. Note that the C' tensor is symmetric ($\sigma_{ij} = \sigma_{ji}$ and thus $C'_{ijkl} = C'_{jikl}$, similarly for the strain tensor), and that the Voigt's notation [104] is typically adopted to simplify eq. (3.12):

$$\sigma_i = C'_{ij}\varepsilon_j, \tag{3.13}$$

with $i, j = 1, 2, \ldots, 6$. Therefore, for any linearly elastic material, the stiffness matrix can be written as

$$C' = \begin{bmatrix} C'_{11} & C'_{12} & C'_{13} & C'_{14} & C'_{15} & C'_{16} \\ C'_{21} & C'_{22} & C'_{23} & C'_{24} & C'_{25} & C'_{26} \\ C'_{31} & C'_{32} & C'_{33} & C'_{34} & C'_{35} & C'_{36} \\ C'_{41} & C'_{42} & C'_{43} & C'_{44} & C'_{45} & C'_{46} \\ C'_{51} & C'_{52} & C'_{53} & C'_{54} & C'_{55} & C'_{56} \\ C'_{61} & C'_{62} & C'_{63} & C'_{64} & C'_{65} & C'_{66} \end{bmatrix} \tag{3.14}$$

MD simulations can be used to apply a deformation $\varepsilon = [\varepsilon_{11}\ \varepsilon_{22}\ \varepsilon_{33}\ 2\varepsilon_{23}\ 2\varepsilon_{13}\ 2\varepsilon_{12}] = [\varepsilon_1\ \varepsilon_2\ \varepsilon_3\ \varepsilon_4\ \varepsilon_5\ \varepsilon_6]$ to a representative unit cell of the material under investigation, and then to measure the respective residual stress in each direction [105]. Given these values, eq. (3.13) allows then to obtain the 6 × 6 elastic stiffness matrix (C') of the simulated material.

The expression of C' is simpler in materials characterized by symmetry, since some of its coefficients are equal to zero. For example, the elastic stiffness tensor of orthotropic materials can be reduced to

$$C' = \begin{bmatrix} C'_{11} & C'_{12} & C'_{13} & 0 & 0 & 0 \\ C'_{21} & C'_{22} & C'_{23} & 0 & 0 & 0 \\ C'_{31} & C'_{32} & C'_{33} & 0 & 0 & 0 \\ 0 & 0 & 0 & C'_{44} & 0 & 0 \\ 0 & 0 & 0 & 0 & C'_{55} & 0 \\ 0 & 0 & 0 & 0 & 0 & C'_{66} \end{bmatrix} \tag{3.15}$$

namely to nine different stiffness coefficients ($C'_{12} = C'_{21}$, $C'_{13} = C'_{31}$, $C'_{23} = C'_{32}$). Instead, the elastic properties of homogeneous isotropic linear elastic materials are determined by two moduli only, namely λ_m and μ_m:

$$\mu_m = \frac{1}{3}(C'_{44} + C'_{55} + C'_{66}) \tag{3.16}$$

and

$$\lambda_m = \frac{1}{3}(C'_{11} + C'_{22} + C'_{33}) - \frac{2}{3}(C'_{44} + C'_{55} + C'_{66}), \tag{3.17}$$

and thus

$$\lambda_m + 2\mu_m = \frac{1}{3}(C'_{11} + C'_{22} + C'_{33}).$$

In this case, the elastic stiffness tensor simplifies to [103]

$$C' = \begin{bmatrix} \lambda_m + 2\mu_m & \lambda_m & \lambda_m & 0 & 0 & 0 \\ \lambda_m & \lambda_m + 2\mu_m & \lambda_m & 0 & 0 & 0 \\ \lambda_m & \lambda_m & \lambda_m + 2\mu_m & 0 & 0 & 0 \\ 0 & 0 & 0 & \mu_m & 0 & 0 \\ 0 & 0 & 0 & 0 & \mu_m & 0 \\ 0 & 0 & 0 & 0 & 0 & \mu_m \end{bmatrix} \tag{3.18}$$

Once λ_m and μ_m are determined, the following relations for homogeneous isotropic linear elastic materials hold:

$$G_m = \mu_m \tag{3.19}$$

$$K_m = \lambda_m + \frac{2}{3}\mu_m \tag{3.20}$$

$$\nu = \frac{\lambda_m}{2(\lambda_m + \mu_m)} \tag{3.21}$$

$$E_m = \mu_m \frac{3\lambda_m + 2\mu_m}{\lambda_m + \mu_m}, \tag{3.22}$$

where G_m is the shear modulus, which regards forces parallel to one surface of the material; K_m is the bulk modulus, which regards the isobaric compression of the material; ν is the Poisson's ratio, which relates the expansion of the material in one direction while it is compressed in another; E_m represents the Young's modulus, which is a measure of the linear elastic stiffness of the material.

MD can be also used to mimic the experimental tensile test of nanomaterials. Typically, the system is first equilibrated; then, a small strain is applied along one longitudinal direction of the computational box with a ramped function of time (see Figure 3.16), and the resulting strain measured [106, 107].

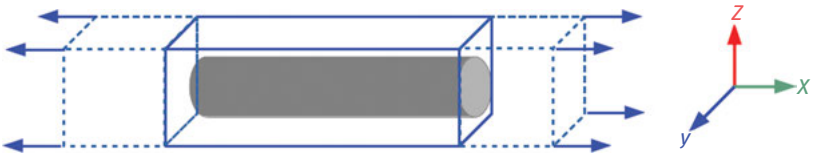

Figure 3.16: Longitudinal deformation of a simulation box.

Electrical properties

Polymeric materials are typically characterized by very low (or no) electrical conductivity; however, the insertion of carbon fillers – such as graphene sheets, CNTs or carbon fibers (CFs) – can improve the electrical properties of the resulting polymer nanocomposites.

A limited volume fraction of CFs has been observed to significantly improve electrical conductivity of polymer nanocomposites [108, 109]. This is due to the formation of continuous conductive networks of CFs in the polymer matrix, thus allowing a transition from nonconductive to conductive electrical properties. The percolation threshold is the critical volume fraction of conductive fillers in the nanocomposite above which conductive pathways in the system always occur. This threshold determines the transition from electrical insulating to conducting behavior, and it is therefore the crucial figure of merit to understand the electrical features of nanocomposites. Furthermore, researchers have reported that the conductive behavior of nanocomposites depends on the spatial distribution of CFs as well. On the one hand, high volume fractions of fibers poorly dispersed in the polymer matrix may lead to fiber agglomeration, which possibly results in electrical conductivity enhancement (but degraded mechanical properties). On the other hand, spatially uniform

distributions of fibers at low volume fractions are unfavorable for the electrical conductance of nanocomposites.

Molecular simulation is an efficient tool to study the electrical properties and percolation mechanism in nanocomposites, since it allows determining whether CFs are forming conductive networks within the polymeric matrix or not. According to the electric tunneling theory, two carbon fillers can be considered as electrically connected to each other if their shortest distance is less than a critical gap, which is known as tunneling distance. The electrical resistance offered by the thin (i.e., less than the tunneling distance) insulating polymer matrix between the conductive fibers is therefore known as tunneling resistance.

The generalized formula for electric tunnel effect through a potential barrier between electrodes separated by a thin insulating film was derived by Simmons in 1963 [110]. Hence, if the thickness of insulating film between the conductive fibers is treated as uniform, the curvature of fibers is neglected, the potential barrier is taken as rectangular and the image forces are included, the current density (j, considered in A/cm^2) flowing through the thin film of polymer matrix between the fibers is given as [110]

$$j = \frac{6.2\times10^{10}}{\Delta s^2}[\phi\exp(-1.025\Delta s\phi^{1/2}) - (\phi+U)\exp(-1.025\Delta s(\phi+U)^{1/2})], \tag{3.23}$$

where

$$\phi = \phi_0 - (U/2s)(s_1+s_2) - \frac{5.75}{\kappa\Delta s}\ln\frac{s_2(s-s_1)}{s_1(s-s_2)}, \tag{3.24}$$

s is the thickness of the insulating polymer film (in Å), $\Delta s = (s_2 - s_1)$ is the difference of the limits of barrier at Fermi level (in Å), κ is the dielectric constant of insulating polymer film, U is the voltage across the insulating polymer film (in V) and ϕ_0 is the height of potential barrier (or work function) (in V). If $U < \phi_0$, then

$$s_1 = 6/\kappa\phi_0$$
$$s_2 = s[1 - 46/(3\phi_0\kappa s + 20 - 2U\kappa s)] + 6/\kappa\phi_0. \tag{3.25}$$

Moreover, the voltage across the insulating polymer film can be calculated as

$$U = e/C = \frac{es}{A_c\kappa\varepsilon_0}, \tag{3.26}$$

where e, C, A_c and ε_0 are electron charge, capacitance, area of the insulating film in contact and permittivity of free space, respectively. The electric tunneling resistance can be finally computed as

$$R_{tunnel} = \frac{U}{j\,A_c}. \tag{3.27}$$

Li et al. [111] performed Monte Carlo simulations to understand the effect of tunneling resistance between CNTs on the electrical conductivity of the whole polymer nanocomposite. Their results indicate that the tunneling resistance increases with the thickness of insulating polymer film (see Figure 3.17). They also reported that the conductivity of nanocomposites drops below 10^{-12} S/m, namely the nanocomposite behaves as an electrical insulator, when the tunneling resistance is larger than 10^{19} Ω. The thickness of polymeric film corresponding to this Ω value is found to be 1.8 nm, which is then considered as the maximum tunneling distance.

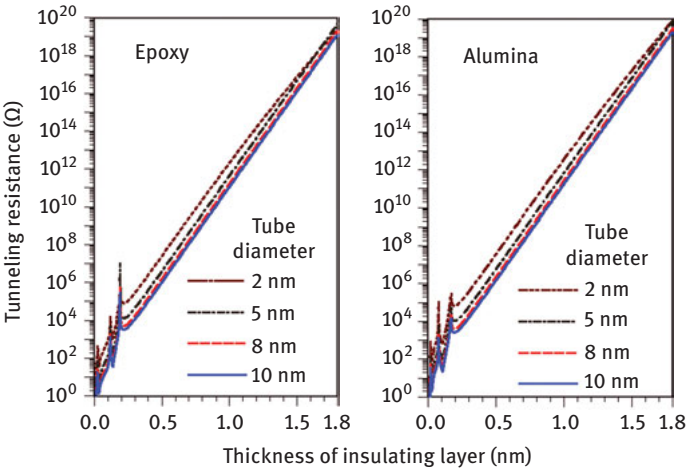

Figure 3.17: Tunneling resistance as a function of the thickness of insulating polymer film between carbon nanotube fillers in a nanocomposite. Different diameters of nanotubes and matrix materials are reported. Reprinted from Ref. [111] with the permission of AIP Publishing.

Hu et al. [112] studied the effect of CNT aspect ratio on the electrical properties of nanocomposites by means of three-dimensional statistical percolation modeling. They reported that the higher aspect ratio of CNTs leads to larger aggregates of fillers in the nanocomposite, which ease the creation of paths with high electrical conductivity. As a result, both lower percolation threshold and higher electrical conductivity of nanocomposites are reported for larger aspect ratio of fillers [112]. Furthermore, the electrical percolation threshold is found to be significantly influenced by the inter-tube van der Waals interaction and tunneling resistance for nanocomposites with low CNT aspect ratio (i.e., length/diameter ratio <200), whereas negligible effects are observed with high aspect ratio [113].

Researchers agree that the tunneling resistance, which shows values several orders of magnitude larger than the intrinsic resistance of carbon fillers, plays a dominating

role in controlling the electrical behavior of nanocomposites [111–114]. Thus, to enhance computational efficiency and simulate larger domains, the intrinsic resistance of nanofillers is often neglected in simulations of nanocomposites with well-dispersed fillers [114].

3.2.2 Mesoscopic models

Thermal properties

The most popular approaches to study effective thermal properties of composites at mesoscale are off-lattice Monte Carlo, dissipative particle dynamics (DPD) and lattice Boltzmann method (LBM).

Duong and coworkers [115] developed an off-lattice Monte Carlo simulation approach to investigate the effective thermal conductivity (λ_{eff}) of CNT-reinforced nanocomposites, taking into account also the thermal boundary resistance (R_k) at CNT–matrix interface. In their model, heat transfer comes from the random motion of a large number of discrete thermal walkers. The proposed model has been widely utilized to investigate the impact of fibers distribution, morphology, volume fraction as well as R_k value at fiber–matrix interface on the λ_{eff} of nanocomposites [116–119], nanofluids [120, 121] and aerogels [122] based on CNTs, with a good capability to reproduce experiments. Kui et al. [123] modified Duong's model to evaluate the thermal properties of composite materials reinforced by graphene sheets. Later, Gong et al. [124–127] extended the initial model to evaluate the thermal conductivity of multiphase composite materials as well. As an example, they studied the λ_{eff} of a polymer composite consisting of polyether ether ketone (PEEK) matrix reinforced by SWCNT fibers and tungsten disulfide (WS_2) nanoparticles [125]. They explored the impact of interfacial thermal resistance at CNT–PEEK and WS_2–PEEK interfaces, CNT morphology (i.e., diameter and aspect ratio of SWCNTs) and SWCNT orientation (i.e., random, parallel or perpendicular to heat flux) on the effective thermal conductivity of composites. According to their findings, λ_{eff} increases with SWCNT concentration, while it decreases with larger Kapitza resistances at the different interfaces. Regarding SWCNT orientation, fibers parallel and perpendicular to the heat flux direction show the best and the worst effect on the overall thermal performance, respectively. They also reported that SWCNTs with higher aspect ratio and smaller diameter generate higher thermal conductivity enhancements at given mass fraction of fillers.

In DPD, the simulated particles (beads) represent whole molecules or fluid regions [128]. For instance, Zhou et al. [129] coupled DPD and smoothed particle hydrodynamics (SPH) to study, at mesoscopic level, the λ_{eff} of polymer composites reinforced by CNTs. This numerical model was used to investigate the impact of different parameters, such as filler dispersion, volume fraction, length and matrix

characteristics, on λ_{eff} of nanocomposites. Their results show that λ_{eff} changes quadratically with the volume fraction of fillers, with both random and aligned distributions of fibers.

LBM is another method that can be used to study the thermal properties of composite materials at mesoscopic level. The most significant advantage of LBM is the easy implementation of different interparticle interactions and complex boundary conditions [130]. Wang and coworkers [131] developed a three-dimensional LBM model to calculate the thermal conductivity of composites reinforced by CFs, in good agreement with experimental evidence. Chiavazzo and Asinari [132], instead, computed through LBM the λ_{eff} of composites made of polypropylene polymer (matrix) and graphite particles (fillers). Fang et al. proposed a multiple relaxation time LBM to predict numerically the λ_{eff} of anisotropic heterogeneous materials, such as polymers reinforced by braiding yarns [133]. The model has been afterward applied to compute longitudinal and perpendicular λ_{eff} of computational domains with different volume fractions of fillers, considering the interfacial thermal resistance between components as well.

Mechanical properties

Atomistic simulation methods are well established for computing the interfacial properties of polymer composites at the molecular level (nanoscale). However, the considerable computational resources required limit the maximum length- and timescale of feasible simulations [134, 135]. While sophisticated strategies for speeding up complex MD simulations of systems that undergo significant configuration changes have been recently suggested on the basis of the equation-free method [136, 137], coarse-grained (CG) models have been specifically developed to simulate polymers [138–140] and carbon fillers (CNTs and graphene) [141, 142].

CG MD overcomes the complexity of atomistic simulations by reducing the degrees of freedom of particle–particle interactions, so that larger length- and timescales (from nanoscale to mesoscale) can be afforded [138, 143]. For the development of CG molecular models, chemically connected atoms are grouped together to form superatoms or CG beads that contain sufficient information to reproduce the chemical features of the molecular structure (see, for instance, Figure 3.18) [139]. Moreover, several methods have been proposed to parametrize the force field among CG beads starting from their respective atomistic details [134, 138, 139]. Arash et al. [143, 144] developed a CG model of CNT/polymer systems, with the aim to compute the mechanical behavior of polymer nanocomposites. Their results confirm that CNT reinforcement significantly enhances the Young's modulus of the composite, and that CG models provide comparable accuracy and lower computational cost than atomistic simulations. Later, Mousavi et al. [145] introduced nonbonded interactions between polymer chains, CNTs and polymer matrix in the CG model to investigate the influence of cross-linking, weight fraction and distribution of CNTs on the elastic properties of polymer nanocomposites.

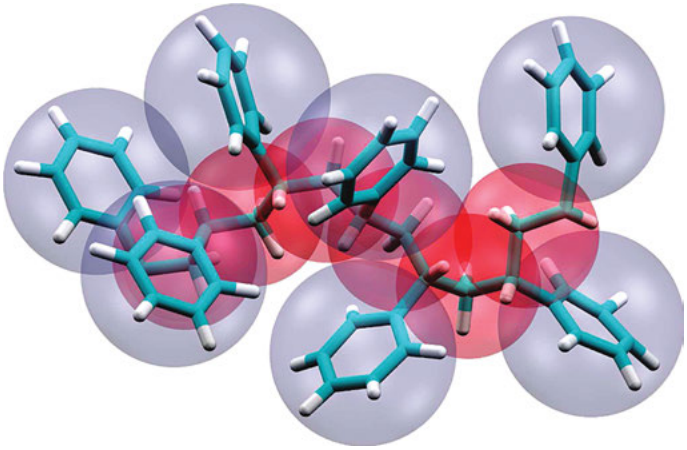

Figure 3.18: Coarse-grained model of polystyrene (red and gray beads) from atomistic details (white and cyan sticks). Reprinted from Ref. [139] with permission of American Chemical Society.

The effect of dispersion, alignment and morphology of nanofillers on the properties of polymer composites can be studied by DPD as well. Zhou et al. [146] studied the dispersion and alignment of CNTs using DPD simulations. Numerical experiments demonstrated that CNTs tend to align themselves in the polymer matrix with increasing nanotube length and volume fraction, especially in well-dispersed systems. Instead, a DPD study on graphene/PMMA (Poly(methyl methacrylate)) composite showed that, while pristine graphene and PMMA are immiscible, high concentrations of graphene functionalizations lead to better filler dispersions in the PMMA matrix [147]. Furthermore, when the volume fraction of fillers is larger, graphene needs to be functionalized more to reach good dispersion. Similar results were obtained by Lin et al. [148], who reported better dispersions of covalently functionalized graphene fillers in PMMA matrix compared to nonfunctionalized ones.

Electrical properties

The RVE concept is also applicable to predict the mesoscale electrical properties of nanocomposites. The electrical conductivity of carbon-based polymer nanocomposites mainly depends on [149–151]:

- the intrinsic electrical conductance of CFs;
- the normal transport through conductive networks of carbon fillers in contact with each other within the polymeric matrix;
- the hopping transport due to the tunneling of electrons between CFs separated by polymer matrix of thickness less than the tunneling distance.

To compute the electrical conductivity of nanocomposites at mesoscale, CFs should be first randomly distributed within a RVE of polymer nanocomposite. These simulations typically assume that fibers have low electrical resistance and thus act as conductors, whereas polymeric matrix is considered as a highly resistive material with low electrical conduction. Therefore, the most conductive path for a given composite is the one minimizing the relative distance between CFs [151, 152]. Different algorithms are available to find the shortest path in a given configuration (e.g., Dijkstra algorithm [153]), which can be thus employed to calculate the electrical conductivity of the simulated nanocomposites at mesoscale. This procedure is typically repeated over different random distributions of fibers in the matrix to reduce statistical fluctuations in terms of composite conductivity.

In a cuboid RVE with dimensions (L_x, L_y, L_z) containing randomly distributed fibers in a polymer matrix [154], each fiber can be modeled as a line segment in spherical coordinates (see Figure 3.19):

$$\begin{aligned} x_i^e &= x_i^s + l_i \sin\theta_i \cos\varphi_i, \\ y_i^e &= y_i^s + l_i \sin\theta_i \sin\varphi_i, \\ z_i^e &= z_i^s + l_i \cos\theta_i, \end{aligned} \tag{3.28}$$

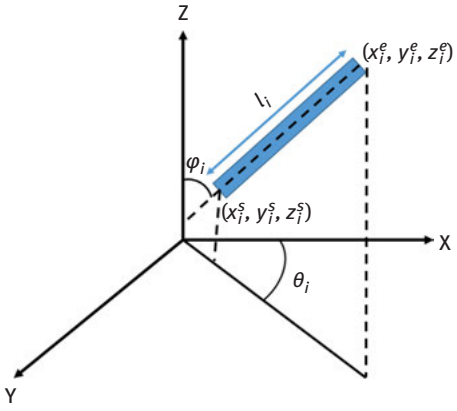

Figure 3.19: Fiber modeled as a line segment in spherical coordinates.

where i is the index of the i^{th} fiber, (x_i^s, y_i^s, z_i^s) and (x_i^e, y_i^e, z_i^e) are the start and end point coordinates of the fiber. The length, polar and azimuthal angle of the i^{th} fiber are denoted as l_i, θ_i and φ_i, respectively.

The start point coordinates, the polar angles and the azimuthal angles of each fiber can be generated randomly as

$$\begin{aligned} x_i^s &= L_x\,\xi, \quad y_i^s = L_y\,\xi, \quad z_i^s = L_z\,\xi \\ \theta_i &= 2\pi\,\xi, \quad \varphi_i = \cos^{-1}(2\xi - 1) \end{aligned} \tag{3.29}$$

where ξ is an uniformly generated random number in the range [0, 1]. To better represent experimental variability, the simulated length of fibers can follow a Weibull distribution [155]. It should be noted that the end points of fibers might initially lie outside the RVE cuboid: in that case, periodic boundary conditions are applied to relocate them inside the cuboid.

The electrical conductivity of nanocomposites can be estimated once the series of resistances in the percolating network is computed, including both intrinsic resistance of fibers (R_{ij}) and their contact resistance ($R_{contact}$). According to the Drude model, the R_{ij} of a fiber (i,j) with l_{ij} length, D diameter and σ_e^{fiber} intrinsic electrical conductivity (see Figure 3.20) can be calculated as [154]

$$R_{ij} = \frac{4l_{ij}}{\sigma_e^{fiber}\pi D^2}. \tag{3.30}$$

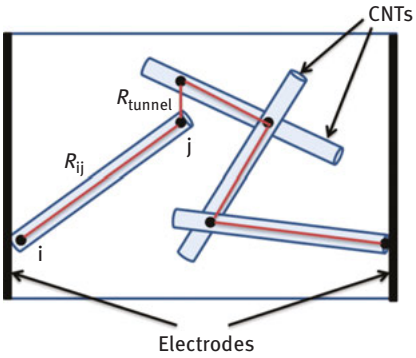

Figure 3.20: Network of electrical resistors in the RVE of a nanocomposite reinforced by nanofillers, for example, CNTs. Reprinted from Ref. [151] with permission from Elsevier.

Considering a marginal effect of temperature, the contact resistance $R_{contact}$ between two fibers can be instead estimated as [150]

$$R_{contact} = \frac{h}{2e^2 M\tau_p}, \tag{3.31}$$

being h the Planck constant, e the electron charge, M the number of conduction channels and τ_p the transmission probability for the electron to tunnel through the polymer layer between fibers. According to Bao et al. [150], the transmission probability τ_p can be estimated by the Wentzel–Kramers–Brillouin approximation [156] as follows:

$$\tau_p = \begin{cases} \exp\left(-\frac{d_{vdW}}{d_{tunnel}}\right) & 0 \le d \le D + d_{vdW} \\ \exp\left(-\frac{d-D}{d_{tunnel}}\right) & D + d_{vdW} \le d \le D + d_{cut} \end{cases} \tag{3.32}$$

where d is the minimum distance between adjacent fibers, d_{vdW} is the van der Waals separation distance and d_{tunnel} is the tunneling length. The latter can be described as [150]

$$d_{tunnel} = \frac{\hbar}{\sqrt{8m_e\Delta E}}, \tag{3.33}$$

where $\hbar = h/2\pi$ is the reduced Planck constant, m_e the mass of electron and ΔE the energy barrier. Note that in eq. (3.32), tunneling effects are neglected if the thickness of polymer matrix between contiguous fibers is larger than d_{cut}, namely, the considered cut-off distance.

Bao et al. [150] studied the effect of CNT alignment in polymer matrix on the critical percolation threshold, and their results revealed that the maximum electrical conductivity is obtained in nanocomposites with partially aligned CNTs. Similarly, Monte Carlo simulations by Zeng et al. [157] reported a clear dependence of the electrical percolation threshold on CNT length, waviness, distribution anisotropy and volume fraction. Improved three-dimensional percolating network theories can also be used to understand how the deformation of CNTs at crossed nanotube junctions influences the electrical conductivity of nanocomposites [158]. In detail, the study by Gong and colleagues [158] suggests that CNT deformation at crossed nanotube junctions determines a large increase in the intrinsic resistance of the nanotube while only a limited decrease in the CNT–CNT contact resistance, therefore, leading to enhanced overall resistance at the junction. Furthermore, numerical simulations based on the Dijkstra algorithm showed that increased contents of MWCNTs in polymer nanocomposites result in higher electrical conductivities, in good quantitative agreement with experiments (see Figure 3.21)

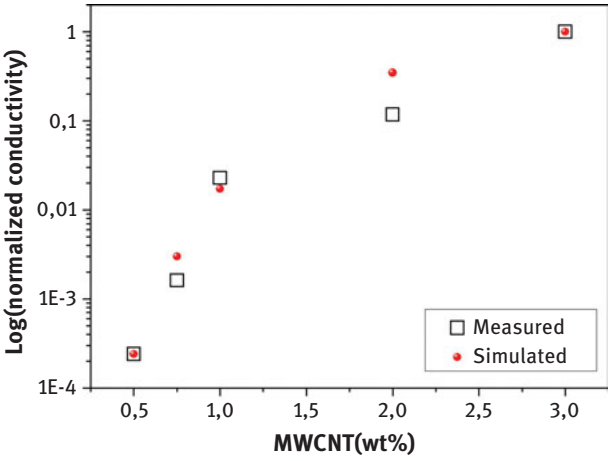

Figure 3.21: Simulation and experimental results of electrical conductivity of CNT-based polymer composites as a function of weight percentage of MWCNTs. Reprinted from Ref. [152] with permission from Elsevier.

[152]. Finally, Rahatekar et al. [159] performed DPD simulations to explore the influence of aspect ratio and fiber alignment on the electrical percolation threshold of nanocomposites.

3.2.3 Continuum models

Thermal properties

The effective thermal conductivity (λ_{eff}) of polymer nanocomposites at macroscale can be predicted by two approaches, namely analytical or simulation ones. Analytical models, for example, effective medium approximation, generally provide quick evaluations of the properties of composites, but cannot take into account neither the interactions between adjacent inclusions nor the actual morphology of composite. Further details on the analytical models for effective thermal conductivity of nanocomposites can be found in a recent review article by Zhai et al. [160].

Due to the current improvement of computational tools and numerical algorithms, finite element method (FEM) has been increasingly utilized to compute the thermal conductivity of composite materials at continuum level. FEM calculates the λ_{eff} of nanocomposites by solving numerically the Fourier's law for conduction at steady state, and this procedure is – in principle – capable to consider different morphologies (e.g., fiber distribution) of the composite material by proper meshing strategies. FEM simulations of composites are typically limited to an RVE of the system. The RVE is built in such a manner that the smallest constituent that can influence the first-order macroscopic behavior of the system is consistent with the simulated length scale; then, the results obtained from the RVE are extended to develop a full-scale model. For example, Figure 3.22 depicts 3D cubic RVEs of composites with different inclusions, namely cylindrical, platelet-like and spherical fillers. The major drawback of FEM in comparison with analytical approaches remains the high computational cost, as well as the modeling complexity given by systems including fibers with high volume fraction or aspect ratio.

Ramani and Vaidynathan [162] carried out an automated finite element analysis to compute λ_{eff} of composite materials. The employed FEM model allowed to study the effect of various parameters, such as fiber aspect ratio, volume fraction, dispersion, orientation and fiber–matrix interfacial thermal resistance on the resulting thermal behavior of composites. Numerical results were compared to analytical models and experiments, finding a good agreement especially at high volume fractions. Ahmed and Masud [163] employed FEM to study the effect of geometrical parameters on the λ_{eff} of polymer composites reinforced by MWCNTs. Their study revealed that the λ of nanocomposites increases with the aspect ratio of nanotubes, whereas interface thermal resistances do not have a prime contribution in lowering the thermal conductivity at the macroscopic scale. Instead, Li et al. [164] quantified

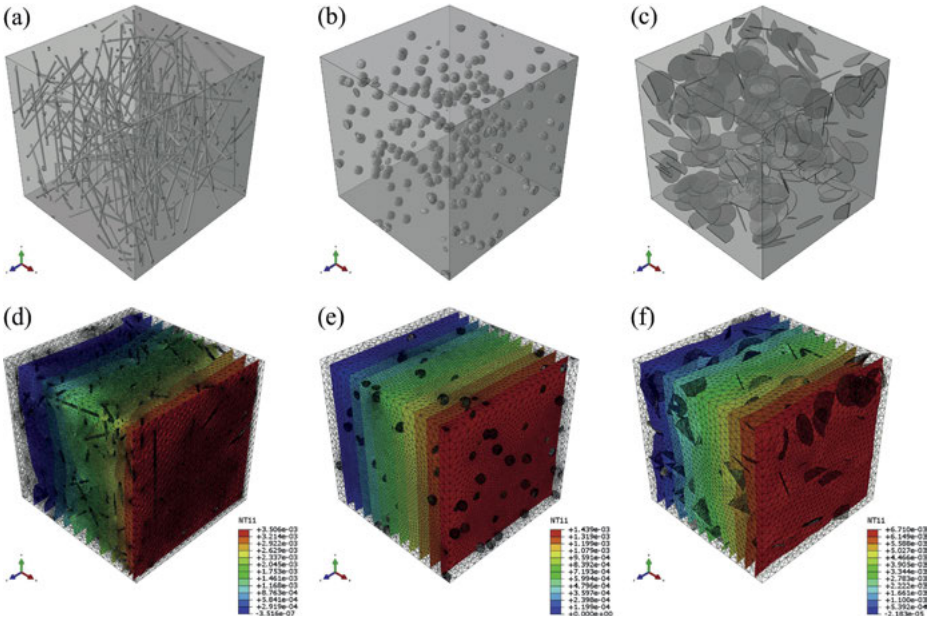

Figure 3.22: Temperature fields in 3D representative volume elements of different composites simulated by FEM method. Reprinted from Ref. [161] with permission from Elsevier.

the influence of SWCNT–matrix interfacial thermal resistance (R_{CNT-m}) on λ_{eff} of SWCNT/polymer composites. Their results showed that the λ_{eff} of composite can be lower than the one of pristine polymer matrix if R_{CNT-m} is greater than a critical value.

Mechanical properties

The FEM can be used to understand the macroscale mechanical properties of nanocomposites, for example, the elastic moduli. At molecular level, the RVE of a generic nanocomposite is a heterogeneous medium consisting of polymer matrix, carbon nanofibers and interface region. However, at continuum level, such heterogeneous RVE should be homogenized to compute the effective material properties through micromechanical analyses (see Figure 3.23). Notice that the homogenization procedure of RVEs to calculate the effective elastic moduli of nanocomposites is equivalent to average the mechanical properties of heterogeneous nanocomposites [165].

The constituents of the RVE can then be assumed as isotropically symmetric within the nanocomposite [166], and the constitutive relation given by the generalized Hooke's law:

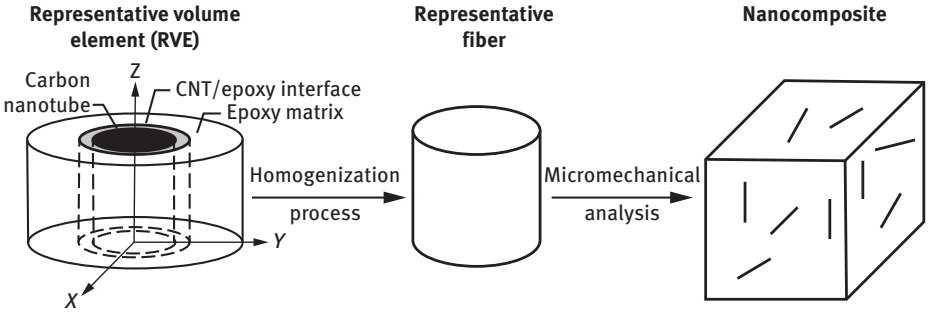

Figure 3.23: Homogenization of a representative volume element of nanocomposite, which includes the nanofiller (CNT), the CNT/epoxy interface and part of the surrounding epoxy matrix into a representative, homogeneous fiber of the composite to be considered for micromechanical analysis. Adapted from Ref. [166] with permission from Elsevier.

$$\sigma_{ij} = C'_{ijkl}\,\varepsilon_{kl}, \qquad i,j,k,l = 1,2,3 \tag{3.34}$$

being C'_{ijkl} the elastic stiffness tensor of the RVE, σ_{ij} and ε_{kl} the stress and strain tensors, respectively. The effective stiffness coefficient $(C'^{\,e}_{ijkl})$ of the homogenized multiconstituent nanocomposite can thus be written as

$$\bar{\sigma}_{ij} = C'^{\,e}_{ijkl}\,\bar{\varepsilon}_{kl}, \tag{3.35}$$

being $\bar{\sigma}_{ij}$ and $\bar{\varepsilon}_{kl}$ the stress and strain tensors averaged over the RVE volume (V_{RVE}), respectively, that is:

$$\bar{\sigma}_{ij} = \frac{1}{V_{RVE}}\int_{V_{RVE}} \sigma_{ij}\mathrm{d}V, \tag{3.36}$$

$$\bar{\varepsilon}_{kl} = \frac{1}{V_{RVE}}\int_{V_{RVE}} \varepsilon_{kl}\mathrm{d}V. \tag{3.37}$$

The effective elastic moduli of nanocomposite are finally calculated using the averaged stress and strain tensors as follows:

$$C'^{\,e}_{ijkl} = \frac{\bar{\sigma}_{ij}}{\bar{\varepsilon}_{kl}}, \quad i=j=k=l \quad (\text{Young's modulus}) \tag{3.38}$$

$$C'^{\,e}_{ijkl} = \frac{\bar{\sigma}_{ij}}{2\bar{\varepsilon}_{kl}}, \quad (i=k)\neq(j=l) \quad (\text{Shear modulus}) \tag{3.39}$$

Instead, the Poisson's ratio of nanocomposite is computed as

$$\nu_{ij} = -\frac{\bar{\varepsilon}_{jj}}{\bar{\varepsilon}_{ii}}. \tag{3.40}$$

Odegard et al. [167] proposed a method to transform the discrete molecular structures of nanotube fillers, polymer matrix and CNT/polymer interface at nanoscale into an equivalent continuum model of composite. Liu and Chen [168] computed the effective mechanical properties of CNT-reinforced composites using a nanoscale RVE and the FEM. They showed that the stiffness of composite increases several times with volume fractions of CNT nanofillers up to 5%. Instead, an equivalent continuum modeling study by Huang and Rodrigue [169] found that both aspect ratio and length of CNT fillers have a significant influence on the mechanical properties of polypropylene-based composites. In a similar study, Kumar and Srivastava [170] reported that the elastic stiffness of polymer matrix was improved by carbon-based filler reinforcements. This study also concluded that graphene reinforcements provided the best in-plane stiffness properties of nanocomposite, whereas CNTs the best out-of-plane ones. Finally, a continuum simulation using multiscale homogenization procedure was applied by Golestanian and Gahruei [171] to understand the effect of CNT waviness on the elastic properties of CNT-reinforced polymer composites. The simulation study revealed that wavier CNTs reduce elastic modulus of nanocomposite along the longitudinal direction, while they increase elastic modulus along the transverse one.

Electrical properties

The effective electrical properties of nanocomposites at the micro- and macroscale are substantially affected by phenomena at molecular level, such as tunneling mechanism and formation of conductive networks.

In case of a 1D conductor with l length and A_c cross section, the effective electrical conductivity of composite (σ_e) can be computed by measuring the electric current (I) flowing through the computational domain, given a certain electric potential (U), that is

$$\sigma_e = \frac{Il}{A_c U}. \tag{3.41}$$

Instead, in case of 3D anisotropic materials, a more general expression should be considered:

$$\mathbf{j} = \sigma_{\mathbf{e}} \mathbf{E}, \tag{3.42}$$

where $\mathbf{j}$ being the current density vector, $\mathbf{E} = -\nabla U$ the electric field vector under electrostatic conditions and $\sigma_{\mathbf{e}}$ the effective conductivity tensor. Typically, FEM analysis with micromechanical corrections is adopted to compute effective electrical properties of nanocomposites at continuum level as, for example, depicted in Figure 3.24.

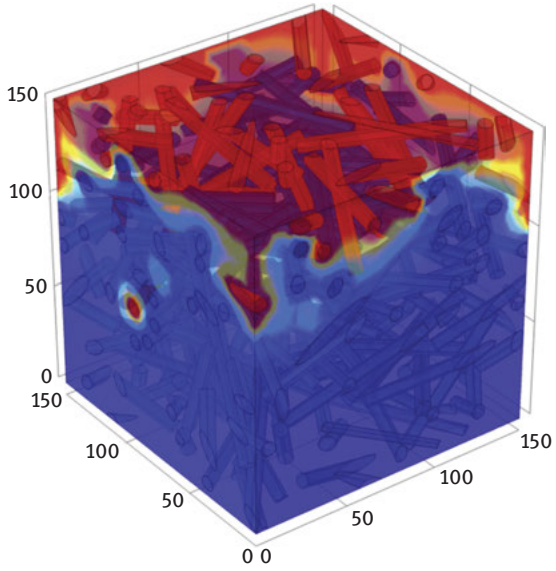

Figure 3.24: Electrical potential within a nanocomposite evaluated by FEM analysis. Reprinted from Ref. [172] with permission from Elsevier.

Seidel and Lagoudas [173] developed a micromechanical model to estimate the electrical properties of CNT–polymer nanocomposites. They reported that the large increment in the σ_e of MWCNT-based nanocomposites at low nanotube concentrations is mainly due to formation of conductive networks, whereas in SWCNT-based nanocomposites, both electron hopping and conductive network formation play a relevant role [173, 174]. The macroscale piezoresistive properties of CNT–polymer composites along both transverse and axial directions were studied instead by Ren and Seidel [37], considering both electric tunneling and inherent piezoresistivity of CNT in the selected RVEs. In that study, the macroscale piezoresistive response of different mesoscale CNT dispersion scenarios in the nanocomposite was predicted using computational micromechanic techniques based on the finite element analysis. The authors found that the electric tunneling mechanism dominates the overall piezoresistive properties of CNT–polymer composites along both transverse and axial directions, whereas the inherent piezoresistivity contribution is more evident along the axial direction rather than along the transverse one [37]. The influence of electric tunneling was found to be negligible in composites with well-dispersed distributions of CNTs, where the intertube distance was larger than the tunneling distance; conversely, agglomerated CNT dispersions eased electric tunneling mechanism.

3.3 Perspectives

The idea to combine different materials to develop an engineered material having unique capabilities, distinct from their constituent materials, is very fascinating, and it has been well known by long time. Nowadays, the possibilities offered by materials processing and, sometimes, nanotechnology have revamped the emphasis on composite materials. In particular, carbon-based composites have already proved to provide remarkable improvements in terms of stiffness, durability, strength and lightweight characteristics in some industrial sectors, for example, automotive.

In spite of the previous successes, some industrial challenges remain for composite materials. According to a recent commentary by *Materials Today* [175], mass production of composites is a key aspect that must still be developed before composites will prove to be useful for many new applications. The lack of mass production/automation techniques sometimes reveals the lack of knowledge of the composite manufacturing process, which forces to rely on try and error in developing new products [175]. Clearly, this approach, which is still dominant in many applications, cannot be properly standardized. Hence, the lack of standardization, design standards and good technical support/backup from suppliers tends to reduce the composite acceptance in an industrial context [175]. Composite materials without a warranty are not well accepted by engineers, who have to deal with high-fidelity standards in the design and production of complex products. Things become even worse in case of recycling CFs, as envisioned by circular economy. End-of-life fiber-reinforced composites are particularly challenging for implementing circular economy, even though some large-scale demonstration has been already funded by the European Commission [176]. All the above factors significantly increase the price of carbon-based composites with regard to their competitors, namely steel, concrete and thermoplastics, and this induces a loss of market share [175]. Price reduction can hardly be achieved by combining raw materials, because this intrinsically requires some additional processing costs. However, one promising alternative option consists in increasing the value chain by adding new functionalities for composite materials. This leads to the so-called smart materials (see Table 3.1 and references therein). Materials with self-sensing and structural health monitoring capabilities, devices with fast triggering shape memory, thermally driven actuators and high-performance all-solid-state supercapacitors are good examples of this strategy. On the other hand, this strategy leads necessarily to even more scientific challenges, because high precision and reproducibility of the arrangement of CFs into the composites are required.

The previous discussion reveals that the exploitation of carbon-based composites requires addressing many scientific challenges, which could benefit from systematic and state-of-the-art materials modeling. Essentially, modeling should address two main issues: (i) elucidating the atomistic details of interface between CF and polymer and (ii) taking into account properly the extreme variability in the CF orientation within the composite.

Table 3.1: Modeling methods for computing thermophysical properties of carbon-based nanocomposites of interest as smart materials. PDMS is polydimethylsiloxane; PVDF is polyvinylidene fluoride.

Material	Modeling method	Properties	Applications as smart material
CNT/PDMS composite	FEM	Structural, mechanical and thermal properties	Thermally driven actuator [181]
CNT/polymer composite	Multiphysics modeling	Electromechanical properties	Strain sensor [182]
CNT/polymer	Percolation network model	Electrical conductivity	High accuracy sensor [183, 184]
PVDF/carbon fiber composite	Multiphysics micromechanics and FEM	Mechanical and piezoelectric properties	Self-sensing and structural health monitoring [39]
CNT sponge/shape memory polymer nanocomposite	FEM	Electrical properties	Fast triggering shape memory material [185]
Graphene oxide (GO)/ reduced GO/water	Quantum/MD simulations	Capacitance	High-performance all-solid-state supercapacitors [186]

The first issue is very well known and is also largely explored from the experimental point of view. For example, CF-reinforced thermoplastic composites gained recent interest due to ease of production and recycling compared to that of thermoset composites, but surface treatments are used to increase the concentration of surface functional groups and hence the fiber–polymer interfacial adhesion [177]. Similarly, different methods of preparation for thermoset composites rely on functionalizing the interface between various nanofillers and epoxy, which is typically characterized by several experimental techniques [178]. Remarkably, nowadays both experimental and modeling techniques are used in order to investigate the relationships between interfacial characteristics and composite properties, for example, with regard to the advantages and disadvantages of covalent and noncovalent functionalization of CFs [179].

The second issue where materials modeling can provide some useful insights is due to the extreme variability in the microscopic structure of composites. Different arrangements of CFs within the composite, shape and orientation of the CF aggregates and dynamics response of the microstructure due to the applied loads are just examples of phenomena that require modeling at scales much larger than that of individual fiber. This may appear simply as a geometrical problem, but it leads immediately to (i) a significant increase in the computational demand and to (ii) a problem of model reduction in postprocessing the modeling results. The second problem is

particularly severe, because it may hinder the opportunity to use materials modeling for increasing the understanding of composites under realistic conditions. In fact, understanding requires squeezing a large amount of information in very simple design guidelines. Moreover, this second problem has an indirect effect on the first problem about affordable computational demand as well. In fact, the possibility to develop simple interpolation models, which can summarize the outcome of more complex models, is essential for any coupling and/or linking strategy. Concerning the latter point, analytical simplified models, which can describe the transfer of energy, mechanical stresses and electricity between neighboring fibers, are highly desirable for developing reliable predictions about percolating networks within the composites. Nowadays, machine learning techniques and artificial intelligence offer solutions for developing analytical interpolating functions, which can be tuned on underlying detailed models and are suitable as input for up-scaled models for predicting macroscopic properties of the materials. These analytical functions keep some insights into the investigated phenomena and, at the same time, are very fast and transferable in up-scaled models, which can describe large portions of the material under investigation. This is a clear advantage with regard to previous techniques based on neural networks. Hence, we envision a huge impact of such techniques in dealing with realistic simulations of carbon-based composites for engineering applications.

Finally, last but not least, carbon-based composites still raise some concerns in terms of their toxicity, particularly when nanofibers are involved. These concerns are about the manufacturing processes of composites, the release of nanoparticles during operation and the end-of-life waste management. Clearly, the fact that some nanofibers, for example, CNTs, are similar in shape and size to asbestos raises further concern [180]. Even though materials modeling may help in assessing some guidelines and in clarifying some scenarios, quantitative and predictive computational nanotoxicology is still far from being mainstream. However, it represents a very interesting approach, which is currently under development in many different fields for assessing preliminarily the impact of new nanotechnologies, and we envision that also carbon-based composites will benefit from it.

Acknowledgments: This work partially received funding from the European Union's Horizon 2020 research and innovation programs, through MODCOMP (grant agreement no. 685844) and SMARTFAN (grant agreement no. 760779) projects.

References

[1] van der Zwaag, S., Self Healing Materials: An Alternative Approach to 20 Centuries of Materials Science, Springer Netherlands: Springer Series in Materials Science, 2007.

[2] Robinson, A. L., Metallurgy: Extraordinary alloys that remember their past. Science 1976, 191, 4230, 934–936.

[3] Jani, J. M., Leary, M., Subic, A., and Gibson, M. A., A review of shape memory alloy research, applications and opportunities. Mater. Des 2014, 56, 1078–1113.
[4] Calkins, F. T., and Mabe, J. H., Shape memory alloy based morphing aerostructures. ASME. J. Mech. Des 2010, 132, 11, 111012.
[5] Baer, G., Wilson, T. S., Matthews, D. L., and Maitland, D. J., Shape memory behavior of thermally stimulated polyurethane for medical applications. J. Appl. Polym. Sci 2007, 103, 6, 3882–3892.
[6] Kim, S., Hawkes, E., Choy, K., Joldaz, M., Foleyz, J., and Wood, R., "Micro artificial muscle fiber using NiTi spring for soft robotics," in 2009 IEEE/RSJ International Conference on Intelligent Robots and Systems, pp 2228–2234, Oct 2009.
[7] Song, G., Ma, N., and Li, H.-N., Applications of shape memory alloys in civil structures. Eng. Struct 2006, 28, 9, 1266–1274.
[8] Gök, M. O., Bilir, M. Z., and Gürcüm, B. H., "Shape-memory applications in textile design," Procedia - Social and Behavioral Sciences, vol. 195, pp. 2160–2169, 2015. World Conference on Technology, Innovation and Entrepreneurship.
[9] Olander, A., An electrochemical investigation of solid cadmium-gold alloys. J. Am. Chem. Soc 1932, 54, 10, 3819–3833.
[10] Buehler, W. J., Gilfrich, J. V., and Wiley, R. C., Effect of low-temperature phase changes on the mechanical properties of alloys near composition TiNi. J. Appl. Phys 1963, 34, 5, 1475–1477.
[11] Otsuka, K., and Ren, X., Physical metallurgy of Ti–Ni-based shape memory alloys. Prog. Mater Sci 2005, 50, 5, 511–678.
[12] van Humbeeck, J., Shape memory materials: State of the art and requirements for future applications. J. Phys. IV France 1997, 07, C5, C5–3–C5–12.
[13] Ratna, D., and Karger-Kocsis, J., Recent advances in shape memory polymers and composites: a review. J. Mater. Sci 2008, 43, 254–269.
[14] Gong, X., Liu, L., Liu, Y., and Leng, J., An electrical-heating and self-sensing shape memory polymer composite incorporated with carbon fiber felt. Smart Mater. Struct 2016, 25, 035036.
[15] Liu, Y., Zhao, J., Zhao, L., Li, W., Zhang, H., Yu, X., and Zhang, Z., High performance shape memory epoxy/carbon nanotube nanocomposites. ACS Appl. Mater. Interfaces 2016, 8, 1, 311–320.
[16] Zhang, Z.-X., Dou, J.-X., He, J.-H., Xiao, C.-X., Shen, L.-Y., Yang, J.-H., Wang, Y., and Zhou, Z.-W., Electrically/infrared actuated shape memory composites based on a bio-based polyester blend and graphene nanoplatelets and their excellent self-driven ability. J. Mater. Chem. C 2017, 5, 4145–4158.
[17] Wang, X., Sparkman, J., and Gou, J., Electrical actuation and shape memory behavior of polyurethane composites incorporated with printed carbon nanotube layers. Compos. Sci. Technol 2017, 141, 8–15.
[18] Yang, E., Xu, Z., Chur, L. K., Behroozfar, A., Baniasadi, M., Moreno, S., Huang, J., Gilligan, J., and Minary-Jolandan, M., Nanofibrous smart fabrics from twisted yarns of electrospun piezopolymer. ACS Appl. Mater. Interfaces 2017, 9, 28, 24220–24229.
[19] Yuan, X., Zhu, S., Li, X., Chen, C., Zhou, K., and Zhang, D., Mechanical performance of piezoelectric fiber composites and electroelastic field concentration near the electrode edges. Mater. Des 2017, 128, Supplement C, 71–79.
[20] Chen, Q., Sun, Y., Qin, L., and Wang, Q. M., Piezoelectric fiber-composite-based cantilever sensor for electric-field-induced strain measurement in soft electroactive polymer. IEEE Trans. Ultrason. Ferroelectr. Freq. Control 2013, 60, 2142–2153.

[21] Lin, X., Huang, S., Zhou, K., and Zhang, D., The influence of structural parameters on the actuation performance of piezoelectric fiber composites. Mater. Des 2016, 107, Supplement C, 123–129.
[22] Yang, Y., Tang, L., and Li, H., Vibration energy harvesting using macrofiber composites. Smart Mater. Struct 2009, 18, 11, 115025.
[23] Zeng, W., Tao, X.-M., Chen, S., Shang, S., Chan, H. L. W., and Choy, S. H., Highly durable all-fiber nanogenerator for mechanical energy harvesting. Energy Environ. Sci 2013, 6, 2631–2638.
[24] Zhong, J., Zhang, Y., Zhong, Q., Hu, Q., Hu, B., Wang, Z. L., and Zhou, J., Fiber-based generator for wearable electronics and mobile medication. ACS Nano 2014, 8, 6, 6273–6280.
[25] Lu, X., Qu, H., and Skorobogatiy, M., Piezoelectric micro- and nanostructured fibers fabricated from thermoplastic nanocomposites using a fiber drawing technique: Comparative study and potential applications. ACS Nano 2017, 11, 2, 2103–2114.
[26] Back cover. Energy Environ. Sci 2013, 6, 2778.
[27] Wang, J., Gao, Y., Zhang, J., and Tian, H., Invisible photochromism and optical anti-counterfeiting based on d-a type inverse diarylethene. J. Mater. Chem. C 2017, 5, 4571–4577.
[28] Ye, J.-T., Wang, L., Wang, H.-Q., Chen, -Z.-Z., Qiu, Y.-Q., and Xie, H.-M., Spirooxazine molecular switches with nonlinear optical responses as selective cation sensors. RSC Adv 2017, 7, 642–650.
[29] Renuka, K. D., Lekshmi, C. L., Joseph, K., and Mahesh, S., Sustainable electronic materials: Reversible phototuning of conductance in a noncovalent assembly of MWCNT and bioresource-derived photochromic molecule. ACS Appl. Mater. Interfaces 2017, 9, 2, 1167–1172.
[30] Wei, J., Jiao, X., Wang, T., and Chen, D., Electrospun photochromic hybrid membranes for flexible rewritable media. ACS Applied Materials & Interfaces 2016, 8, 43, 29713–29720.
[31] William J, S., "Doll or the like," Oct. 27 1953. US Patent 2656647 A.
[32] Ercole, F., Davis, T. P., and Evans, R. A., Photo-responsive systems and biomaterials: photochromic polymers, light-triggered self-assembly, surface modification, fluorescence modulation and beyond. Polym. Chem 2010, 1, 37–54.
[33] Manouras, T., and Vamvakaki, M., Field responsive materials: photo-, electro-, magnetic- and ultrasound-sensitive polymers. Polym. Chem 2017, 8, 74–96.
[34] Fasano, M., Chiavazzo, E., and Asinari, P., Water transport control in carbon nanotube arrays. Nanoscale research letters 2014, 9, 1, 559.
[35] Gizzatov, A., Key, J., Aryal, S., Ananta, J., Cervadoro, A., Palange, A. L., Fasano, M., Stigliano, C., Zhong, M., Di, M. D., Guven, A., Chiavazzo, E., Asinari, P., Liu, X., Ferrari, M., Wilson, L. J., and Decuzzi, P., Hierarchically structured magnetic nanoconstructs with enhanced relaxivity and cooperative tumor accumulation. Adv. Funct. Mater 2014, 24, 29, 4584–4594.
[36] Chiavazzo, E., Fasano, M., Asinari, P., and Decuzzi, P., Scaling behaviour for the water transport in nanoconfined geometries. Nat. Commun 2014, 5, 3565.
[37] Ren, X., and Seidel, G. D., Computational micromechanics modeling of piezoresistivity in carbon nanotube–polymer nanocomposites. Compos. Interfaces 2013, 20, 9, 693–720.
[38] Ren, X., Burton, J., Seidel, G. D., and Lafdi, K., Computational multiscale modeling and characterization of piezoresistivity in fuzzy fiber reinforced polymer composites. Int. J. Solids Struct 2015, 54, 121–134.
[39] Greminger, M., and Haghiashtiani, G., Multiscale modeling of PVDF matrix carbon fiber composites. Modell. Simul. Mater. Sci. Eng 2017, 25, 4, 045007.
[40] Toth, R., Santese, F., Pereira, S. P., Nieto, D. R., Pricl, S., Fermeglia, M., and Posocco, P., Size and shape matter! A multiscale molecular simulation approach to polymer nanocomposites. Journal of Materials Chemistry 2012, 22, 12, 5398–5409.

[41] Posocco, P., Pricl, S., and Fermeglia, M., Multiscale modeling approach for polymeric nanocomposites. Modeling and Prediction of Polymer Nanocomposite Properties 2013, 95–128.
[42] Fermeglia, M., Posocco, P. and Pricl, S., Nano tools for macro problems: multiscale molecular modeling of nanostructured polymer systems. Composite Interfaces 2013, 20, 6, 379–394.
[43] Subramanian, N., Rai, A., and Chattopadhyay, A., Atomistically informed stochastic multiscale model to predict the behavior of carbon nanotube-enhanced nanocomposites. Carbon 2015, 94, 661–672.
[44] Laurini, E., Posocco, P., Fermeglia, M., and Pricl, S., Modena nanotools: An integrated multiscale simulation workflow to predict thermophysical properties of thermoplastic polyurethanes. Journal of Computational Science 2016, 15, 24–33.
[45] Khromov, K. Y., Knizhnik, A., Potapkin, B., and Kenny, J., Multiscale modeling of electrical conductivity of carbon nanotubes based polymer nanocomposites. Journal of Applied Physics 2017, 121, 22, 225102.
[46] Laurini, E., Marson, D., Fermeglia, M., and Pricl, S., Multimodel approach for accurate determination of industry-driven properties for polymer nanocomposite materials. Journal of computational science 2018, 26, 28–38.
[47] Li, Y., and Seidel, G., Multiscale modeling of the interface effects in CNT-epoxy nanocomposites. Computational Materials Science 2018, 153, 363–381.
[48] De Baas, A., "What makes a material function? let me compute the ways . . .," Modeling in FP7 NMP Programme, European Commission, vol. 6th edition, 2017.
[49] The CEN Workshop Agreement, "CEN/WS MODA - Materials modelling - terminology, classification and metadata," CWA, vol. 17284, 2018. ftp://ftp.cencenelec.eu/CEN/Sectors/TCandWorkshops/Workshops/WS%20MODA/CWA_17284.pdf.
[50] Ghedini, E., Hashibon, A., Friis, J., Goldbeck, G., Schmitz, G., and de Baas, A., "EMMO the European Materials Modelling Ontology," in EMMC Workshop on Interoperability in Materials Modelling, 2017. https://emmc.info/wp-content/uploads/2017/12/EMMC_IntOp2017-Cambridge_Ghedini_Bologna.pdf.
[51] Sáenz Ezquerro, C., Laspalas, M., Chiminelli, A., Serrano, F., and Valero, C., Interface characterization of epoxy resin nanocomposites: A molecular dynamics approach. Fibers 2018, 6, 3, 54.
[52] Humphrey, W., Dalke, A., and Schulten, K., VMD: Visual molecular dynamics. J. Mol. Graphics 1996, 14, 1, 33–38.
[53] Hanwell, M. D., Curtis, D. E., Lonie, D. C., Vandermeersch, T., Zurek, E., and Hutchison, G. R., Avogadro: an advanced semantic chemical editor, visualization, and analysis platform. J. Cheminf. Aug 2012, 4, 17.
[54] Fasano, M., Crisafulli, A., Cardellini, A., Bergamasco, L., Chiavazzo, E., and Asinari, P., Thermally triggered nanorocket from double-walled carbon nanotube in water. Molecular Simulation 2019, 45, 4–5, 417–424.
[55] Schulz, M., and Frisch, H. L., Monte Carlo studies of interpenetrating polymer network formation. J. Chem. Phys 1994, 101, 11, 10008–10022.
[56] Doherty, D., Holmes, B., Leung, P., and Ross, R., Polymerization molecular dynamics simulations. i. cross-linked atomistic models for poly (methacrylate) networks. Comput. Theor. Polym. Sci 1998, 8, 1–2, 169–178.
[57] Yarovsky, I., and Evans, E., Computer simulation of structure and properties of crosslinked polymers: application to epoxy resins. Polymer 2002, 43, 3, 963–969.
[58] Li, C., and Strachan, A., Molecular simulations of crosslinking process of thermosetting polymers. Polymer 2010, 51, 25, 6058–6070.

[59] Jang, C., Lacy, T. E., Gwaltney, S. R., Toghiani, H., and Pittman, C. U. Jr, Relative reactivity volume criterion for cross-linking: Application to vinyl ester resin molecular dynamics simulations. Macromolecules 2012, 45, 11, 4876–4885.
[60] Varshney, V., Patnaik, S. S., Roy, A. K., and Farmer, B. L., A molecular dynamics study of epoxy-based networks: Cross-linking procedure and prediction of molecular and material properties. Macromolecules 2008, 41, 18, 6837–6842.
[61] Lin, P.-H., and Khare, R., Molecular simulation of cross-linked epoxy and epoxy-POSS nanocomposite. Macromolecules 2009, 42, 12, 4319–4327.
[62] Rottach, D. R., Curro, J. G., Budzien, J., Grest, G. S., Svaneborg, C., and Everaers, R., Molecular dynamics simulations of polymer networks undergoing sequential cross-linking and scission reactions. Macromolecules 2007, 40, 1, 131–139.
[63] Wu, C., and Xu, W., Atomistic molecular modelling of crosslinked epoxy resin. Polymer 2006, 47, 16, 6004–6009.
[64] Jang, C., Sirk, T. W., Andzelm, J. W., and Abrams, C. F., Comparison of crosslinking algorithms in molecular dynamics simulation of thermosetting polymers. Macromol. Theory Simul 2015, 24, 3, 260–270.
[65] Maiti, A., Mahan, G., and Pantelides, S., Dynamical simulations of nonequilibrium processes—heat flow and the Kapitza resistance across grain boundaries. Solid State Commun 1997, 102, 7, 517–521.
[66] Kubo, R., Toda, M., and Hashitsume, N., Statistical physics II: nonequilibrium statistical mechanics, Vol. 31. Springer Science & Business Media, 2012.
[67] Evans, D. J., and Morriss, G. P., 4 - The Green–Kubo relations, In: Statistical Mechanics of Nonequilibrium Liquids (D. J. Evans and G. P. Morrisseds.), 77–93, Academic Press, 1990.
[68] Kumar, A., Sundararaghavan, V., and Browning, A., Study of temperature dependence of thermal conductivity in cross-linked epoxies using molecular dynamics simulations with long range interactions. Modell. Simul. Mater. Sci. Eng 2014, 22, 2, 025013.
[69] Sirk, T. W., Karim, M., Khare, K. S., Lenhart, J. L., Andzelm, J. W., and Khare, R., Bi-modal polymer networks: composition-dependent trends in thermal, volumetric and structural properties from molecular dynamics simulation. Polymer 2015, 58, 199–208.
[70] Fasanella, N. A., and Sundararaghavan, V., Atomistic modeling of thermal conductivity of epoxy nanotube composites. JOM 2016, 68, 5, 1396–1410.
[71] Anderson, C. V., and Tamma, K. K., An overview of advances in heat conduction models and approaches for prediction of thermal conductivity in thin dielectric films. Int. J. Numer. Methods Heat Fluid Flow 2004, 14, 1, 12–65.
[72] Müller-Plathe, F., A simple nonequilibrium molecular dynamics method for calculating the thermal conductivity. J. Chem. Phys 1997, 106, 14, 6082–6085.
[73] Varshney, V., Patnaik, S. S., Roy, A. K., and Farmer, B. L., Heat transport in epoxy networks: A molecular dynamics study. Polymer 2009, 50, 14, 3378–3385.
[74] Mortazavi, B., Benzerara, O., Meyer, H., Bardon, J., and Ahzi, S., Combined molecular dynamics-finite element multiscale modeling of thermal conduction in graphene epoxy nanocomposites. Carbon 2013, 60, 356–365.
[75] Alaghemandi, M., Müller-Plathe, F., and Böhm, M. C., Thermal conductivity of carbon nanotube—polyamide-6,6 nanocomposites: Reverse nonequilibrium molecular dynamics simulations. J. Chem. Phys 2011, 135, 18, 11B606.
[76] Shen, Z., Bateman, S., Wu, D. Y., McMahon, P., Dell'Olio, M., and Gotama, J., The effects of carbon nanotubes on mechanical and thermal properties of woven glass fibre reinforced polyamide-6 nanocomposites. Compos. Sci. Technol 2009, 69, 2, 239–244.

[77] Du, F., Guthy, C., Kashiwagi, T., Fischer, J. E., and Winey, K. I., An infiltration method for preparing single-wall nanotube/epoxy composites with improved thermal conductivity. J. Polym. Sci., Part B: Polym. Phys 2006, 44, 10, 1513–1519.
[78] Tascini, A. S., Armstrong, J., Chiavazzo, E., Fasano, M., Asinari, P., and Bresme, F., Thermal transport across nanoparticle-fluid interfaces: the interplay of interfacial curvature and nanoparticle-fluid interactions. Phys. Chem. Chem. Phys 2017, 19, 3244–3253.
[79] Fasano, M., Bigdeli, M. B., Sereshk, M. R. V., Chiavazzo, E., and Asinari, P., Thermal transmittance of carbon nanotube networks: Guidelines for novel thermal storage systems and polymeric material of thermal interest. Renewable Sustainable Energy Review 2015, 41, 1028–1036.
[80] Bigdeli, M. B., and Fasano, M., Thermal transmittance in graphene based networks for polymer matrix composites. Int. J. Therm. Sci 2017, 117, 98–105.
[81] Shenogin, S., Xue, L., Ozisik, R., Keblinski, P., and Cahill, D. G., Role of thermal boundary resistance on the heat flow in carbon-nanotube composites. J. Appl. Phys 2004, 95, 12, 8136–8144.
[82] Lervik, A., Bresme, F., and Kjelstrup, S., Heat transfer in soft nanoscale interfaces: the influence of interface curvature. Soft Matter 2009, 5, 2407–2414.
[83] Varshney, V., Roy, A. K., Michalak, T. J., Lee, J., and Farmer, B. L., Effect of curing and functionalization on the interface thermal conductance in carbon nanotube–epoxy composites. Jom 2013, 65, 2, 140–146.
[84] Shenogin, S., Bodapati, A., Xue, L., Ozisik, R., and Keblinski, P., Effect of chemical functionalization on thermal transport of carbon nanotube composites. Appl. Phys. Lett 2004, 85, 12, 2229–2231.
[85] Clancy, T. C., and Gates, T. S., Modeling of interfacial modification effects on thermal conductivity of carbon nanotube composites. Polymer 2006, 47, 16, 5990–5996.
[86] Liu, C., and Fan, S., Effects of chemical modifications on the thermal conductivity of carbon nanotube composites. Appl. Phys. Lett 2005, 86, 12, 123106.
[87] Shen, X., Wang, Z., Wu, Y., Liu, X., and Kim, J.-K., Effect of functionalization on thermal conductivities of graphene/epoxy composites. Carbon 2016, 108, 412–422.
[88] Luo, T., and Lloyd, J. R., Enhancement of thermal energy transport across graphene/graphite and polymer interfaces: a molecular dynamics study. Adv. Funct. Mater 2012, 22, 12, 2495–2502.
[89] Wang, Y., Yang, C., Pei, Q.-X., and Zhang, Y., Some aspects of thermal transport across the interface between graphene and epoxy in nanocomposites. ACS Appl. Mater. Interfaces 2016, 8, 12, 8272–8279.
[90] Zheng, Q., Xue, Q., Yan, K., Gao, X., Li, Q., and Hao, L., Effect of chemisorption on the interfacial bonding characteristics of carbon nanotube–polymer composites. Polymer 2008, 49, 3, 800–808.
[91] Varshney, V., Patnaik, S. S., Roy, A. K., and Farmer, B. L., Modeling of thermal conductance at transverse cnt- cnt interfaces. J. Phys. Chem. C 2010, 114, 39, 16223–16228.
[92] Clancy, T. C., Frankland, S.-J. V., Hinkley, J. A., and Gates, T. S., Multiscale modeling of thermal conductivity of polymer/carbon nanocomposites. Int. J. Therm. Sci 2010, 49, 9, 1555–1560.
[93] Varshney, V., Roy, A. K., and Baur, J. W., Modeling the role of bulk and surface characteristics of carbon fiber on thermal conductance across the carbon-fiber/matrix interface. ACS Appl. Mater. Interfaces 2015, 7, 48, 26674–26683.
[94] Huang, H., Chen, L., Varshney, V., Roy, A. K., and Kumar, S., Investigation of phonon transport and thermal boundary conductance at the interface of functionalized swcnt and poly (ether-ketone). Journal of Applied Physics 2016, 120, 9, 095102.

[95] Wang, Y., Zhan, H., Xiang, Y., Yang, C., Wang, C. M., and Zhang, Y., Effect of covalent functionalization on thermal transport across graphene–polymer interfaces. J. Phys. Chem. C 2015, 119, 22, 12731–12738.
[96] Kim, B., Choi, J., Yang, S., Yu, S., and Cho, M., Multiscale modeling of interphase in crosslinked epoxy nanocomposites. Composites Part B: Engineering 2017, 120, 128–142.
[97] Kuang, Y., and Huang, B., Effects of covalent functionalization on the thermal transport in carbon nanotube/polymer composites: a multi-scale investigation. Polymer 2015, 56, 563–571.
[98] Zhang, J., Jiang, C., Jiang, D., and Peng, H.-X., Nano-engineering thermal transport performance of carbon nanotube networks with polymer intercalation: a molecular dynamics study. Phys. Chem. Chem. Phys 2014, 16, 9, 4378–4385.
[99] Hida, S., Hori, T., Shiga, T., Elliott, J., and Shiomi, J., Thermal resistance and phonon scattering at the interface between carbon nanotube and amorphous polyethylene. Int. J. Heat Mass Transfer 2013, 67, 1024–1029.
[100] Carlborg, C. F., Shiomi, J., and Maruyama, S., Thermal boundary resistance between single-walled carbon nanotubes and surrounding matrices. Phys. Rev. B 2008, 78, 20, 205406.
[101] Chawla, R., Mechanical and tribological properties of graphene reinforced natural rubber composites: A molecular dynamics study. MRS Advances 2018, 3, 10, 525–530.
[102] Weerasinghe, A., Lu, C.-T., Maroudas, D., and Ramasubramaniam, A., Multiscale shear-lag analysis of stiffness enhancement in polymer–graphene nanocomposites. ACS applied materials & interfaces 2017, 9, 27, 23092–23098.
[103] Theodorou, D. N., and Suter, U. W., Atomistic modeling of mechanical properties of polymeric glasses. Macromolecules jan 1986, 19, 139–154.
[104] Weiner, J. H., Statistical mechanics of elasticity, New York: Wiley, 1983.
[105] Li, Y., Wang, S., and Wang, Q., A molecular dynamics simulation study on enhancement of mechanical and tribological properties of polymer composites by introduction of graphene. Carbon 2017, 111, 538–545.
[106] Zaminpayma, E., Molecular dynamics simulation of mechanical properties and interaction energy of polythiophene/polyethylene/poly (pphenylenevinylene) and CNTs composites. Polymer Composites 2014, 35, 11, 2261–2268.
[107] Sul, J.-H., Prusty, B. G., and Kelly, D. W., Application of molecular dynamics to evaluate the design performance of low aspect ratio carbon nanotubes in fibre reinforced polymer resin. Composites Part A: Applied Science and Manufacturing 2014, 65, 64–72.
[108] Coleman, J. N., Curran, S., Dalton, A. B., Davey, A. P., McCarthy, B., Blau, W., and Barklie, R. C., Percolation-dominated conductivity in a conjugated-polymer-carbon-nanotube composite. Phys. Rev. B Sep 1998, 58, R7492–R7495.
[109] Ahmad, K., Pan, W., and Shi, S.-L., Electrical conductivity and dielectric properties of multiwalled carbon nanotube and alumina composites. Appl. Phys. Lett 2006, 89, 13, 133122.
[110] Simmons, J. G., Generalized formula for the electric tunnel effect between similar electrodes separated by a thin insulating film. J. Appl. Phys 1963, 34, 6, 1793–1803.
[111] Li, C., Thostenson, E. T., and Chou, T.-W., Dominant role of tunneling resistance in the electrical conductivity of carbon nanotube–based composites. Appl. Phys. Lett 2007, 91, 22, 223114.
[112] Hu, N., Masuda, Z., Yan, C., Yamamoto, G., Fukunaga, H., and Hashida, T., The electrical properties of polymer nanocomposites with carbon nanotube fillers. Nanotechnology 2008, 19, 21, 215701.
[113] Lu, W., Chou, T.-W., and Thostenson, E. T., A three-dimensional model of electrical percolation thresholds in carbon nanotube-based composites. Appl. Phys. Lett 2010, 96, 22, 223106.

[114] Yu, Y., Song, G., and Sun, L., Determinant role of tunneling resistance in electrical conductivity of polymer composites reinforced by well dispersed carbon nanotubes. J. Appl. Phys 2010, 108, 8, 084319.
[115] Duong, H. M., Papavassiliou, D. V., Lee, L. L., and Mullen, K. J., Random walks in nanotube composites: Improved algorithms and the role of thermal boundary resistance. Appl. Phys. Lett 2005, 87, 1, 013101.
[116] Duong, H. M., Papavassiliou, D. V., Mullen, K. J., and Maruyama, S., Computational modeling of the thermal conductivity of single-walled carbon nanotube–polymer composites. Nanotechnology 2008, 19, 6, 065702.
[117] Duong, H. M., Yamamoto, N., Papavassiliou, D. V., Maruyama, S., and Wardle, B. L., Inter-carbon nanotube contact in thermal transport of controlled-morphology polymer nanocomposites. Nanotechnology 2009, 20, 15, 155702.
[118] Bui, K., Grady, B. P., and Papavassiliou, D. V., Heat transfer in high volume fraction CNT nanocomposites: Effects of inter-nanotube thermal resistance. Chem. Phys. Lett 2011, 508, 4, 248–251.
[119] Bui, K., Grady, B. P., Saha, M. C., and Papavassiliou, D. V., Effect of carbon nanotube persistence length on heat transfer in nanocomposites: A simulation approach. Appl. Phys. Lett 2013, 102, 20, 203116.
[120] Duong, H. M., Papavassiliou, D. V., Mullen, K. J., Wardle, B. L., and Maruyama, S., Calculated thermal properties of single-walled carbon nanotube suspensions. J. Phys. Chem. C 2008, 112, 50, 19860–19865.
[121] Duong, H. M., Papavassiliou, D. V., Mullen, K. J., Wardle, B. L., and Maruyama, S., A numerical study on the effective thermal conductivity of biological fluids containing single-walled carbon nanotubes. Int. J. Heat Mass Transfer 2009, 52, 23, 5591–5597.
[122] Gong, F., Tam, Y. S., Nguyen, S. T., and Duong, H. M., Prediction of thermal resistances and heat conduction of carbon nanotube aerogels in various permeated gases. Chem. Phys. Lett 2015, 627, 116–120.
[123] Bui, K., Duong, H. M., Striolo, A., and Papavassiliou, D. V., Effective heat transfer properties of graphene sheet nanocomposites and comparison to carbon nanotube nanocomposites. J. Phys. Chem. C 2011, 115, 10, 3872–3880.
[124] Gong, F., Papavassiliou, D. V., and Duong, H. M., Off-lattice Monte Carlo simulation of heat transfer through carbon nanotube multiphase systems taking into account thermal boundary resistances. Numerical Heat Transfer, Part A 2014, 65, 11, 1023–1043.
[125] Gong, F., Bui, K., Papavassiliou, D. V., and Duong, H. M., Thermal transport phenomena and limitations in heterogeneous polymer composites containing carbon nanotubes and inorganic nanoparticles. Carbon 2014, 78, 305–316.
[126] Gong, F., Hongyan, Z., Papavassiliou, D. V., Bui, K., Lim, C., and Duong, H. M., Mesoscopic modeling of cancer photothermal therapy using single-walled carbon nanotubes and near infrared radiation: insights through an off-lattice Monte Carlo approach. Nanotechnology 2014, 25, 20, 205101.
[127] Gong, F., Duong, H. M., and Papavassiliou, D. V., Inter-carbon nanotube contact and thermal resistances in heat transport of three-phase composites. J. Phys. Chem. C 2015, 119, 14, 7614–7620.
[128] Gooneie, A., Schuschnigg, S., and Holzer, C., A review of multiscale computational methods in polymeric materials. Polymers 2017, 9, 1, 16.
[129] Zhou, B., Luo, W., Yang, J., Duan, X., Wen, Y., Zhou, H., Chen, R., and Shan, B., Thermal conductivity of aligned CNT/polymer composites using mesoscopic simulation. Composites Part A: Applied Science and Manufacturing 2016, 90, 410–416.

[130] Raabe, D., Overview of the Lattice Boltzmann method for nano-and microscale fluid dynamics in materials science and engineering. Modell. Simul. Mater. Sci. Eng 2004, 12, 6, R13.
[131] Wang, M., Kang, Q., and Pan, N., Thermal conductivity enhancement of carbon fiber composites. Appl. Therm. Eng 2009, 29, 2, 418–421.
[132] Chiavazzo, E., and Asinari, P., Reconstruction and modeling of 3d percolation networks of carbon fillers in a polymer matrix. Int. J. Therm. Sci 2010, 49, 12, 2272–2281.
[133] Fang, W.-Z., Chen, L., Gou, -J.-J., and Tao, W.-Q., Predictions of effective thermal conductivities for three-dimensional four-directional braided composites using the Lattice Boltzmann method. International Journal of Heat and Mass Transfer 2016, 92, 120–130.
[134] Reith, D., Meyer, H., and Müller-Plathe, F., Mapping atomistic to coarse-grained polymer models using automatic simplex optimization to fit structural properties. Macromolecules 2001, 34, 7, 2335–2345.
[135] Rzepiela, A. J., Louhivuori, M., Peter, C., and Marrink, S. J., Hybrid simulations: combining atomistic and coarse-grained force fields using virtual sites. Phys. Chem. Chem. Phys 2011, 13, 10437–10448.
[136] Chiavazzo, E., Covino, R., Coifman, R. R., Gear, C. W., Georgiou, A. S., Hummer, G., and Kevrekidis, I. G., Intrinsic map dynamics exploration for uncharted effective free-energy landscapes. Proceedings of the National Academy of Sciences 2017, 114, 28, E5494–E5503.
[137] Georgiou, A. S., Bello-Rivas, J. M., Gear, C. W., Wu, H.-T., Chiavazzo, E., and Kevrekidis, I. G., An exploration algorithm for stochastic simulators driven by energy gradients. Entropy 2017, 19, 7, 294.
[138] Dirk, R., Mathias, P., and Florian, M., Deriving effective mesoscale potentials from atomistic simulations. J. Comput. Chem 2003, 24, 13, 1624–1636.
[139] Fritz, D., Harmandaris, V. A., Kremer, K., and van der Vegt, N. F. A., Coarse-grained polymer melts based on isolated atomistic chains: Simulation of polystyrene of different tacticities. Macromolecules 2009, 42, 19, 7579–7588.
[140] Hsu, D. D., Xia, W., Arturo, S. G., and Keten, S., Systematic method for thermomechanically consistent coarse-graining: A universal model for methacrylate-based polymers. J. Chem. Theory Comput 2014, 10, 6, 2514–2527.
[141] Zhao, J., Jiang, J.-W., Wang, L., Guo, W., and Rabczuk, T., Coarse-grained potentials of single-walled carbon nanotubes. J. Mech. Phys. Solids 2014, 71, 197–218.
[142] Ruiz, L., Xia, W., Meng, Z., and Keten, S., A coarse-grained model for the mechanical behavior of multi-layer graphene. Carbon 2015, 82, 103–115.
[143] Arash, B., Park, H. S., and Rabczuk, T., Mechanical properties of carbon nanotube reinforced polymer nanocomposites: A coarse-grained model. Composites Part B: Engineering 2015, 80, 92–100.
[144] Arash, B., Park, H. S., and Rabczuk, T., Tensile fracture behavior of short carbon nanotube reinforced polymer composites: A coarse-grained model. Compos. Struct 2015, 134, 981–988.
[145] Mousavi, A. A., Arash, B., Zhuang, X., and Rabczuk, T., A coarse-grained model for the elastic properties of cross linked short carbon nanotube/polymer composites. Composites Part B: Engineering 2016, 95, 404–411.
[146] Zhou, B., Luo, W., Yang, J., Duan, X., Wen, Y., Zhou, H., Chen, R., and Shan, B., Simulation of dispersion and alignment of carbon nanotubes in polymer flow using dissipative particle dynamics. Comput. Mater. Sci 2017, 126, 35–42.
[147] Ju, S.-P., Wang, Y.-C., Huang, G.-J., and Chang, J.-W., Miscibility of graphene and poly(methyl methacrylate) (PMMA): molecular dynamics and dissipative particle dynamics simulations. RSC Adv 2013, 3, 8298–8307.

[148] Lin, F., Yang, C., Zeng, Q., and Xiang, Y., Morphological and mechanical properties of graphene-reinforced PMMA nanocomposites using a multiscale analysis. Comput. Mater. Sci 2018, 150, 107–120.
[149] Kilbride, B. E., Coleman, J. N., Fraysse, J., Fournet, P., Cadek, M., Drury, A., Hutzler, S., Roth, S., and Blau, W. J., Experimental observation of scaling laws for alternating current and direct current conductivity in polymer-carbon nanotube composite thin films. J. Appl. Phys 2002, 92, 7, 4024–4030.
[150] Bao, W., Meguid, S., Zhu, Z., Pan, Y., and Weng, G., A novel approach to predict the electrical conductivity of multifunctional nanocomposites. Mech. Mater 2012, 46, Supplement C, 129–138.
[151] Grabowski, K., Zbyrad, P., Uhl, T., Staszewski, W. J., and Packo, P., Multiscale electro-mechanical modeling of carbon nanotube composites. Comput. Mater. Sci 2017, 135C, 169–180.
[152] Castellino, M., Rovere, M., Shahzad, M. I., and Tagliaferro, A., Conductivity in carbon nanotube polymer composites: A comparison between model and experiment. Composites Part A 2016, 87, Supplement C, 237–242.
[153] Dijkstra, E., A note on two problems in connexion with graphs. Numer. Math 1959, 1, 1, 269–271.
[154] Bao, W. S., Meguid, S. A., Zhu, Z. H., and Weng, G. J., Tunneling resistance and its effect on the electrical conductivity of carbon nanotube nanocomposites. J. Appl. Phys 2012, 111, 9, 093726.
[155] Wang, S., Liang, Z., Wang, B., and Zhang, C., Statistical characterization of single-wall carbon nanotube length distribution. Nanotechnology 2006, 17, 3, 634.
[156] Bohm, D., Quantum Theory, Dover Publications: Dover Books on Physics, 1989.
[157] Zeng, X., Xu, X., Shenai, P. M., Kovalev, E., Baudot, C., Mathews, N., and Zhao, Y., Characteristics of the electrical percolation in carbon nanotubes/polymer nanocomposites. J. Phys. Chem. C 2011, 115, 44, 21685–21690.
[158] Gong, S., Zhu, Z. H., and Haddad, E. I., Modeling electrical conductivity of nanocomposites by considering carbon nanotube deformation at nanotube junctions. J. Appl. Phys 2013, 114, 7, 074303.
[159] Rahatekar, S. S., Hamm, M., Shaffer, M. S. P., and Elliott, J. A., Mesoscale modeling of electrical percolation in fiber-filled systems. J. Chem. Phys 2005, 123, 13, 134702.
[160] Zhai, S., Zhang, P., Xian, Y., Zeng, J., and Shi, B., Effective thermal conductivity of polymer composites: Theoretical models and simulation models. Int. J. Heat Mass Transfer 2018, 117, 358–374.
[161] He, B., Mortazavi, B., Zhuang, X., and Rabczuk, T., Modeling Kapitza resistance of two-phase composite material. Compos. Struct 2016, 152, Supplement C, 939–946.
[162] Ramani, K., and Vaidyanathan, A., Finite element analysis of effective thermal conductivity of filled polymeric composites. J. Compos. Mater 1995, 29, 13, 1725–1740.
[163] Ahmed, S., and Masud, A., "Evaluation of effective thermal conductivity of multiwalled carbon nanotube reinforced polymer composites using finite element method and continuum model," Procedia Eng., vol. 90, pp.129–135, 2014. 10th International Conference on Mechanical Engineering, ICME 2013.
[164] Li, X., Fan, X., Zhu, Y., Li, J., Adams, J. M., Shen, S., and Li, H., Computational modeling and evaluation of the thermal behavior of randomly distributed single-walled carbon nanotube/polymer composites. Comput. Mater. Sci 2012, 63, 207–213.
[165] Srivastava, A., and Kumar, D., A continuum model to study interphase effects on elastic properties of CNT/GS-nanocomposite. Mater. Res. Express 2017, 4, 2, 025036.
[166] Wernik, J., and Meguid, S., Multiscale micromechanical modeling of the constitutive response of carbon nanotube-reinforced structural adhesives. Int. J. Solids Struct 2014, 51, 14, 2575–2589.

[167] Odegard, G., Gates, T., Wise, K., Park, C., and Siochi, E., Constitutive modeling of nanotube–reinforced polymer composites. Compos. Sci. Technol 2003, 63, 11, 1671–1687.
[168] Liu, Y., and Chen, X., Evaluations of the effective material properties of carbon nanotube-based composites using a nanoscale representative volume element. Mech. Mater 2003, 35, 1, 69–81.
[169] Huang, J., and Rodrigue, D., Equivalent continuum models of carbon nanotube reinforced polypropylene composites. Materials & Design 2013, 50, 936–945.
[170] Kumar, D., and Srivastava, A., Elastic properties of CNT-and graphene-reinforced nanocomposites using RVE. Steel and Composite Structures 08 2016, 21, 1085–1103.
[171] Golestanian, H., and Gahruei, M. H., Effective mechanical properties of nanocomposites reinforced with wavy carbon nanotubes. Mater. Sci. Technol 2013, 29, 8, 913–920.
[172] Nilsson, F., Krückel, J., Schubert, D. W., Chen, F., Unge, M., Gedde, U. W., and Hedenqvist, M. S., Simulating the effective electric conductivity of polymer composites with high aspect ratio fillers. Compos. Sci. Technol 2016, 132, 16–23.
[173] Seidel, G. D., and Lagoudas, D. C., A micromechanics model for the electrical conductivity of nanotube-polymer nanocomposites. J. Compos. Mater 2009, 43, 9, 917–941.
[174] Feng, C., and Jiang, L., Micromechanics modeling of the electrical conductivity of carbon nanotube (CNT)–polymer nanocomposites. Compos. A Appl. Sci. Manuf 2013, 47, Supplement C, 143–149.
[175] Jacob, A., "What is the biggest challenge facing the composites industry today?," Plastics magazine, Materials Today, 2013. https://www.materialstoday.com/composite-industry/comment/what-is-the-biggest-challenge-facing-the-composite/.
[176] FiberEUse, "Large scale demonstration of new circular economy value chains based on the reuse of end-of-life fiber reinforced composites," CORDIS Europe, vol. 730323, 2017–2021. https://cordis.europa.eu/project/rcn/210178_en.html.
[177] Yao, -S.-S., Jin, F.-L., Rhee, K. Y., Hui, D., and Park, S.-J., Recent advances in carbon-fiber-reinforced thermoplastic composites: A review. Composites Part B: Engineering 2017, 142, 241–250.
[178] Gantayat, S., Rout, D., and Swain, S. K., Carbon nanomaterial–reinforced epoxy composites: A review. Polymer-Plastics Technology and Engineering 2018, 57, 1, 1–16.
[179] Chen, J., Yan, L., Song, W., and Xu, D., Interfacial characteristics of carbon nanotube-polymer composites: A review. Composites Part A: Applied Science and Manufacturing 2018, 114, 149–169.
[180] Chernova, T., Murphy, F. A., Galavotti, S., Sun, X.-M., Powley, I. R., Grosso, S., Schinwald, A., Zacarias-Cabeza, J., Dudek, K. M., Dinsdale, D., Quesne, J. L., Bennett, J., Nakas, A., Greaves, P., Poland, C. A., Donaldson, K., Bushell, M., Willis, A. E., and MacFarlane, M., Long-fiber carbon nanotubes replicate asbestos-induced mesothelioma with disruption of the tumor suppressor gene Cdkn2a (ink4a/Arf). Current Biology 2017, 27, 21, .e6, 3302–3314.
[181] Zhang, W., Chen, L., Zhang, J., and Huang, Z., Design and optimization of carbon nanotube/polymer actuator by using finite element analysis. Chinese Physics B 2017, 26, 4, 048801.
[182] Grabowski, K., Blacha, I., Staszewski, W. J., Uhl, T., and Packo, P., Optimization of multi-scale modelling of CNT/polymer composite strain sensors, In: Health Monitoring of Structural and Biological Systems 2017, Vol. 10170, 101700R, International Society for Optics and Photonics, 2017.
[183] Gong, S., Wang, Y., Xiao, Z., Li, Z., Wang, Z. X., Lei, R. S., and Zhu, Z. H., Effect of temperature on the electrical property of epoxy composites with carbon nanotube. Compos. Sci. Technol 2017, 149, 48–54.

[184] Gong, S., Wu, D., Li, Y., Jin, M., Xiao, T., Wang, Y., Xiao, Z., Zhu, Z., and Li, Z., Temperature-independent piezoresistive sensors based on carbon nanotube/polymer nanocomposite. Carbon 2018, 137, 188–195.

[185] Zhou, G., Zhang, H., Xu, S., Gui, X., Wei, H., Leng, J., Koratkar, N., and Zhong, J., Fast triggering of shape memory polymers using an embedded carbon nanotube sponge network. Sci. Rep 2016, 6, 24148.

[186] Gao, Y., Wan, Y., Wei, B., and Xia, Z., Capacitive enhancement mechanisms and design principles of high-performance graphene oxide-based all-solid-state supercapacitors. Adv. Funct. Mater 2018, 28, 17, 1706721.